CHALMERS
UNIVERSITY OF TECHNOLOGY

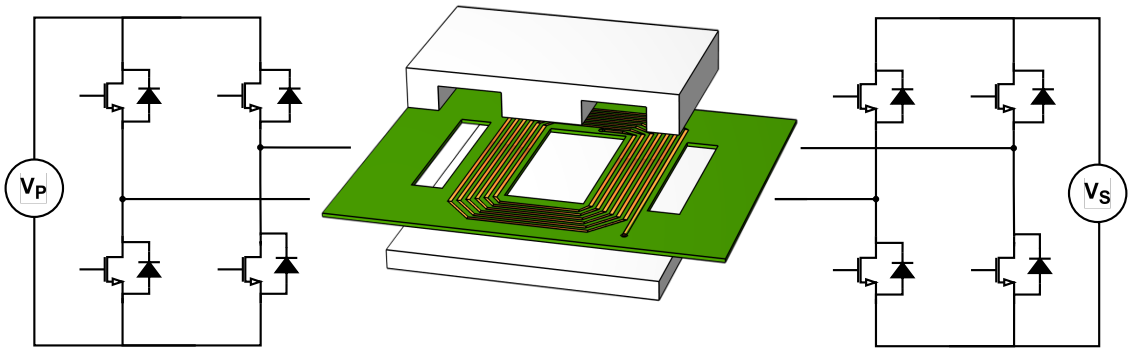

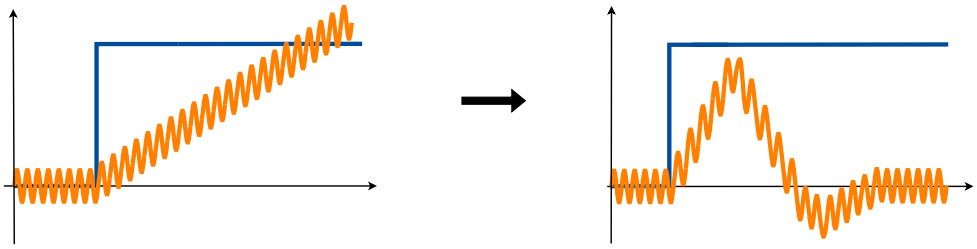

Active Transformer Flux Balancing for a PSFB-DAB Converter

Implementation of active flux balancing on a planar transformer in a PSFB-DAB onverter for DCDC application

Master's thesis in Sustainable Electric Power Engineering and Electromobility

Philip Axelsson
Awaz Nabi Pour

DEPARTMENT OF ELECTRICAL ENGINEERING
CHALMERS UNIVERSITY OF TECHNOLOGY
Gothenburg, Sweden 2025
www.chalmers.se

Master's thesis 2025

Active Transformer Flux Balancing for a PSFB-DAB converter

Implementation of Active Flux Balancing on a Planar Transformer in a PSFB-DAB converter for DCDC application

PHILIP AXELSSON
AWAZ NABI POUR

CHALMERS
UNIVERSITY OF TECHNOLOGY

Department of Electrical Engineering
Division of Sustainable Electric Power Engineering and Electromobility
Chalmers University of Technology
Gothenburg, Sweden 2025

Active Transformer Flux Balancing for a PSFB-DAB converter
Implementation of Active Flux Balancing on a Planar Transformer in a PSFB-DAB converter for DCDC application
Philip Axelsson
Awaz Nabi Pour

Supervisors:
Spyros Gryparis - Aros Electronics
Rafael Bausone - Chalmers University of Technology
Examiner:
Torbjörn Thiringer - Chalmers University of Technology: Department of Electrical Engineering

Master's Thesis 2025
Department of Electrical engineering
Division of Sustainable Electric Power Engineering and Electromobility
Chalmers University of Technology
SE-412 96 Gothenburg
Telephone +46 31 772 1000

Cover: Visualization of a PSFB-DAB converter featuring a planar transformer separating the two H-bridges, along with a simplified representation of the active balancing effect on the magnetizing current.

Typeset in LaTeX
Printed by Chalmers Reproservice
Gothenburg, Sweden 2025

Active Transformer Flux Balancing for a PSFB-DAB converter
Implementation of Active Flux Balancing on a Planar Transformer in a PSFB-DAB converter for DCDC application
Philip Axelsson
Awaz Nabi Pour
Department of Electrical engineering
Chalmers University of Technology

Abstract

This thesis investigates the implementation of active flux balancing on a planar transformer within a PSFB-DAB converter system. This is used to mitigate magnetizing flux and prevent transformer core saturation. The approach starts with the creation of a state-space model of the transformer, followed by the development of two PI-based controllers including a flux balancing controller and a DC offset controller. A hybrid control approach was also briefly investigated. The worst-case operating scenario for the system was examined considering component variations, temperature effects, changes in primary and secondary voltages and phase shifts. This was then used to evaluate the worst-case operating conditions to determine the maximum offset the controller could handle while still preventing saturation. The results show that the converter can handle a maximum voltage step of 4.9 V for the worst case operating condition of, $V_p = 850$, $V_s = 550$ and $\varphi = -90°$.

Keywords: Planar transformer, PSFB-DAB, DAB, Active flux balancing, current control, control system, PI-control, DC-DC application, state-space, PWM

Acknowledgements

We would like to express our sincere gratitude to the following individuals who have provided invaluable support and guidance throughout the course of this thesis.

First and foremost, we would like to thank our supervisor, Spyros Gryparis, for your expert guidance, constant encouragement, and essential feedback throughout this Thesis. Your knowledge and dedication has been crucial in shaping this work.

We would like to express our gratitude to our examiner, Torbjörn Thiringer, for your valuable time, effort, and constructive feedback during the evaluation of this thesis. Your insights have greatly enhanced the quality of this work.

We would also like to thank our supervisor, Rafael Bausone. Your expertise and assistance in LTspice and circuit analysis significantly contributed to the success of this project. Your constructive suggestions and willingness to help is greatly appreciated.

Lastly we would like to extend a great thank you to all the people working at Aros electronics, who have welcomed us and supported us throughout the entirety of this thesis. Thank you.

Philip Axelsson & Awaz Nabi Pour, Gothenburg, May 2025

List of Acronyms

Below is the list of acronyms that have been used throughout this thesis listed in alphabetical order:

AC	Alternating Current
DAB	Dual Active Bridge
DC	Direct Current
FIR	Finite Impulse Response
GBW	Gain Bandwidth
Gm	Gain Margin
IC	Integrated Circuit
KCL	Kirchhoff's Current Law
KVL	Kirchhoff's Voltage Law
LTI	Linear Time Invariant
MMF	Magnetomotive Force
MOSFET	Metal Oxide Semiconductor Field Effect Transistor
Op-amp	Operational Amplifier
PCB	Printed Circuit Board
PI	Proportional–Integral
PSFB-DAB	Phase Shift Full Bridge Dual Active Bridge
PV	Photovoltaic
PWM	Pulse Width Modulation
RC filter	Resistor Capacitor Filter
SPICE	Simulation Program with Integrated Circuit Emphasis
TPS	Triple Phase Shift

Contents

1
Introduction

In today's ever-evolving world, the demand for electrical power continues to increase rapidly. The growing loads on the electrical grid such as electric vehicles and appliances, along with the rise of renewable energy sources all contribute to this increased demand [1]. The variable nature of renewable energy sources such as photovoltaic (PV) and wind leads to the need for energy storage systems. To manage the power flow between these sources, DC-DC power converters play an important role. This creates a demand for new engineering solutions to meet these new requirements. By enhancing the performance of existing power electronics technology a lot of energy and money can be saved.

This section of the report will introduce background to the topic, the aim of the report, the objective and scope as well as the limitations for the project.

1.1 Background

With the global transition towards green energy the development in industries such as electromobility and smart-grids have increased dramatically. This increased need for energy storage systems such as batteries has lead to an increased interest in Dual Active Bridge (DAB) converters thanks to their versatility and efficiency.

To galvanically isolate two different DC links in the DAB topology a high frequency transformer is used in the converter. This transformer protects the DC links from faults in the connecting circuit such as undesired current flow, noise and voltage spikes at the cost of increased component costs [2].

In high-frequency transformer applications, it is crucial to regulate the magnetic flux in the core to prevent saturation. Traditional passive methods such as operating at low duty cycles or using a DC-blocking capacitor to eliminate offset current can help reduce core saturation. However, these approaches often come with significant trade-offs, including the need for bulky capacitors which mainly add both size and cost, making them unsuitable for applications where factors such as size, cost, weight, and power density are critical. An alternative is active flux balancing, which adjusts the duty cycles on the primary and secondary sides to cancel out DC bias, effectively preventing core saturation without compromising performance.

The focus of this thesis is to implement and analyze a working active flux bal-

ancing method for a high frequency Phase Shifted Full-Bridge Dual Active Bridge (PSFB-DAB) converter. The design and implementation of the required amplification circuits as well as parameter dependencies will also investigated.

1.2 Aim

This thesis aims to implement and investigate active flux balancing on a PSFB-DAB converter and its effect on transformer core saturation. This was done by utilizing simulation in MATLAB Simulink to establish the performance of the flux balancing method. The method will also be implemented and tested on hardware provided by Aros electronics AB.

1.2.1 Objective and Scope

In order to accomplish this the system and transformer are modeled and evaluated in Simulink. Control systems to adjust the duty cycles on the primary and secondary side of the transformer will also be implemented in Simulink. Amplification circuits for the currents will be modeled and evaluated in LTspice.

The ability to eliminate the DC-bias current responsible for saturating the transformer was investigated. The impact of different converter operating conditions and measurement accuracy on the active flux balancing performance was also evaluated.

1.3 Limitations

This thesis is limited to primarily investigate one active flux balancing method and some variations of its implementation. Factors that will be evaluated for the different variations of active flux balancing will be limited to flux levels, size and cost to more effectively analyze the performance of the method.

2

Theory

In this chapter, a theoretical background is introduced to allow the methods and results to be better understood. The functionality of the PSFB-DAB converter will be explained as well as the relevant theory for the flux balancing control and circuit designs.

2.1 PSFB-DAB converter

The PSFB-DAB is a dual active bidirectional DC-DC converter with a full bridge configuration on the primary and secondary sides [3]. Figure 2.1 shows a simplified circuit model of a PSFB-DAB converter. The gate signals control the high frequency switching of the MOSFETs in the full bridge circuits, which in turn is used to convert the voltage from DC to a square wave modulation resembling an AC voltage. This then passes through the transformer and is converted back to DC [3].

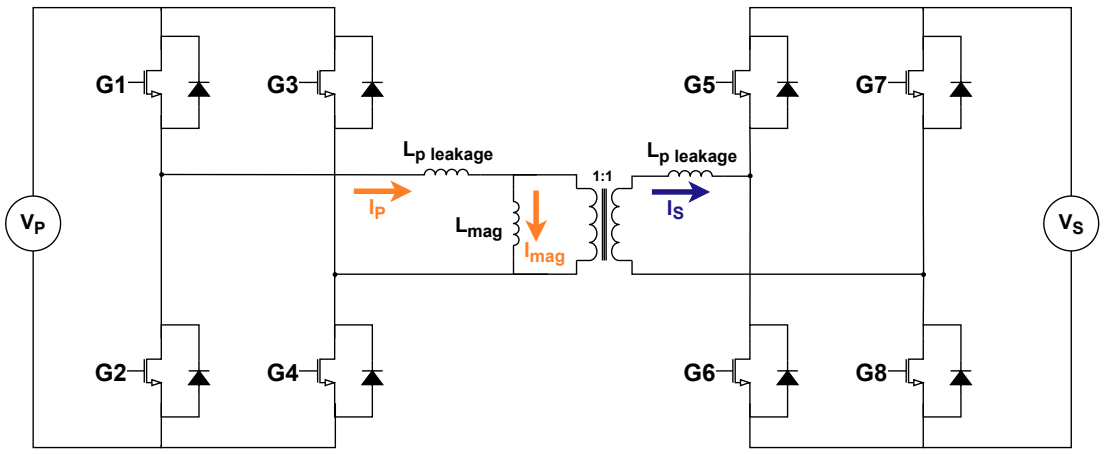

Figure 2.1: Schematic of PSFB-DAB converter

The primary-side voltage is controlled using gate signals G1, G2, G3, and G4, while the secondary-side voltage is regulated by gate signals G5, G6, G7, and G8. The overall voltage waveform of the full bridge representing the differential voltage seen by the transformer is determined by the combined switching behavior of the MOSFETs, as illustrated in Figure 2.2. Corresponding switching patterns are available on both sides of the transformer and are applied selectively based on the chosen control strategy.

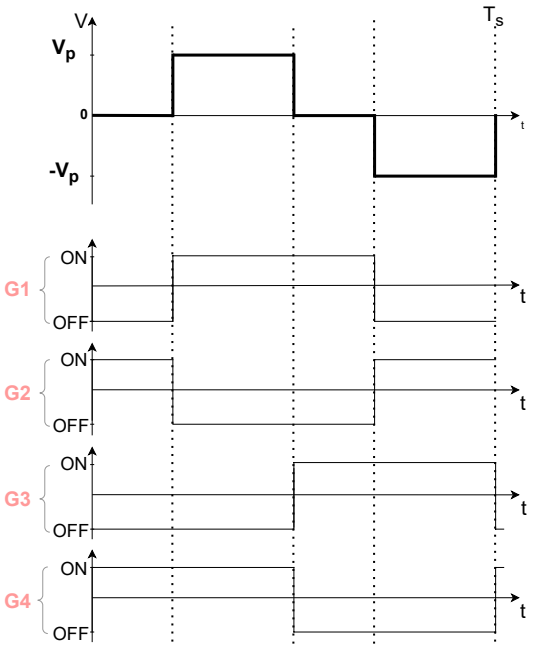

Figure 2.2: Switching pattern of the MOSFETs and resulting voltage

The PSFB-DAB converter has three degrees of freedom when it comes to controlling the power flow from the primary to the secondary side. The duty cycles for the primary and secondary side as well as the inter-bridge phase shift are adaptable to decide the primary and secondary side voltages and as a result the amount and direction of power transfer respectively. This gives the converter advantages such as controllable bi-directional power transfer, zero-voltage switching, fast dynamic response, symmetric structure and modularity [4], [5].

Figure 2.3 shows how the primary side duty cycle D_p, secondary side duty cycle D_s, and inter-bridge phase shift φ, are defined in this thesis.

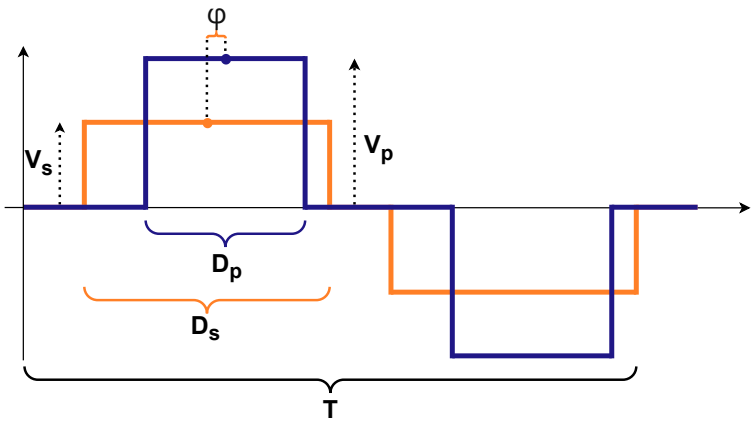

Figure 2.3: Definitions of phase shifts

To increase efficiency and optimize power transfer, Triple Phase Shift (TPS) modulation is used [6]. TPS modulation is an advanced control technique used in PSFB-DAB converters. By adjusting these three phase shifts independently, TPS modulation allows several degrees of freedom. This can be used to optimize the converter for a wide range of voltage and power levels. TPS modulation can reduce circulating currents, minimize switching losses hence maximizing the efficiency of the converter for a specific operating point.

In the following sections of the report, slight adjustments to the duty cycles will be defined using two control signals: d_{fb} and d_{dc} which are added to the gate signals of the converter. A visual representation of this configuration is provided in Figure 4.22.

2.2 Planar transformer

Planar transformers are made for high frequency applications that utilize flat windings which most often are traces on a PCB instead of copper wire wound around the cores. These flat conductors increase the available operating frequency as the flat conductors are less limited by the skin effect. Figure 2.4 shows a render of a planar transformer and how the core material fits into the PCB.

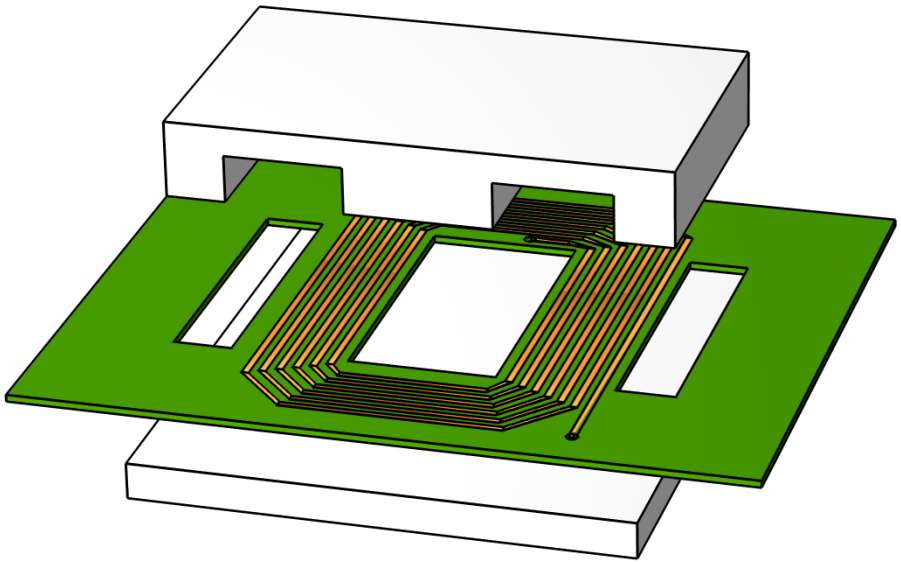

Figure 2.4: Render of a planar transformer

This architecture also provides a lower profile which generally is 1/4 to 1/2 of the height of a wire wound transformer [7]. The thermal characteristic and power density of the transformer are also improved due to the increased surface to volume ratio which helps increase the heat transfer of the transformer [7]. Additionally the

interconnection between arbitrary layers inside multilayer PCBs provide significant reduction in leakage inductance and high-frequency winding losses, improving the efficiency of the transformer [7]. There are several advantages of a planar transformer compared to a wire wound transformer including ease of manufacturability, cost reduction, repeatability and modularity. Some disadvantages of a planar transformer are larger footprints, higher winding capacitance and limited number of turns.

2.2.1 Magnetic saturation in a transformer

Magnetic saturation in a transformer core occurs when the magnetic flux density B [Wb/m^2] no longer increases, even as the magnetic field intensity H [A/m] continues to rise [8]. This happens because the magnetic domains within the core material become fully aligned with the external field. Once all domains are saturated and cannot reorient further, B reaches its maximum value, and additional increases in H have no further effect on the flux density.

Figure 2.5a shows a typical hysteresis curve and the path it takes for increasing and decreasing H. In Figure 2.5b the saturation regions are marked red and can be seen where the curve starts to flatten and become non-linear.

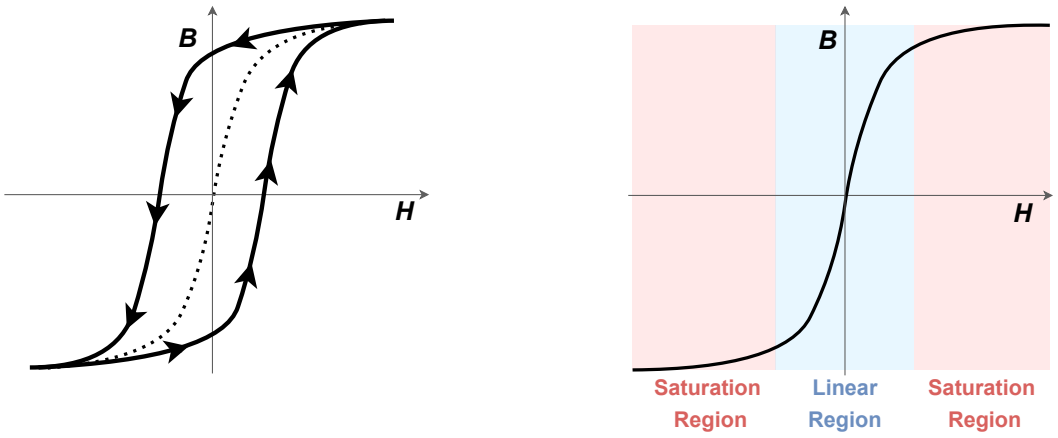

(a) Hysteresis curve

(b) Hysteresis curve showing saturation regions

Figure 2.5: Hysteresis curves

Figure 2.6 shows how the magnetizing current increases when a DC component is added to the flux density [9], [10]. Typically the DC offset in the magnetic flux density becomes smaller if the equivalent series resistance of the transformer circuit is larger [11]. To reduce conduction losses, the series resistance is kept as low as possible which means that a small DC component in the applied voltage will generate a large DC flux density component. This results in that the flux easily is being driven out of the B-H curves linear region.

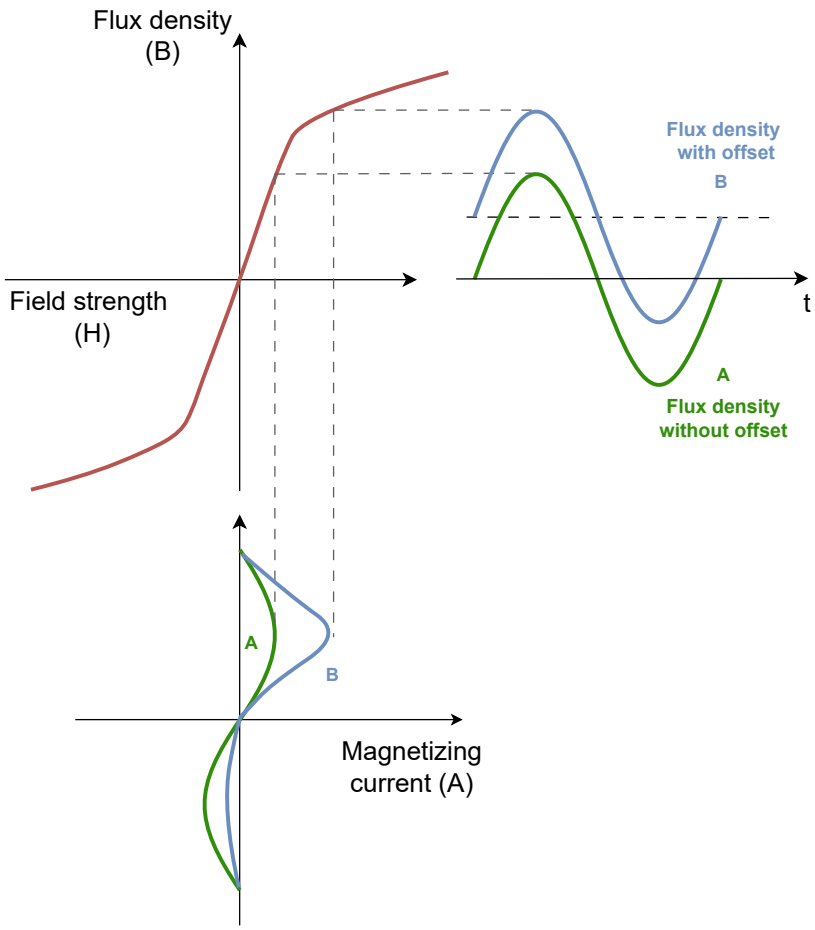

Figure 2.6: Relation between flux density and magnetizing current

When operating outside the linear region, increased conduction and switching losses occur which cause reduced efficiency of the converter coupled with increased operational temperatures of both semiconductors and the transformer [11]. Additionally a DC biased flux density waveform will result in more core losses which contributes to reducing the efficiency further [12].

2.3 Transformer flux balancing

Flux balancing methods are used to prevent saturation of the transformer core by controlling the magnetic flux in the transformer. There are two main types of flux balancing, passive and active flux balancing. Passive flux balancing mainly utilizes the electrical properties of added components to balance the flux in the transformer core without adding control circuits, while active flux balancing uses various real-time control systems to adjust the flux in the transformer.

2.3.1 Passive flux balancing methods

One of the most common and simple passive flux balancing methods is the addition of DC-blocking capacitors. The capacitors are connected in series with both the primary and secondary side windings [13] and are used to remove the DC part of the voltage signals that cause an offset in the transformer flux [14]. This is however unsuitable for most high-power applications due to the increase in converter size, losses, cost and the introduced slow dynamic responses [15]. Figure 2.7 shows how the DC-blocking capacitor can be implemented.

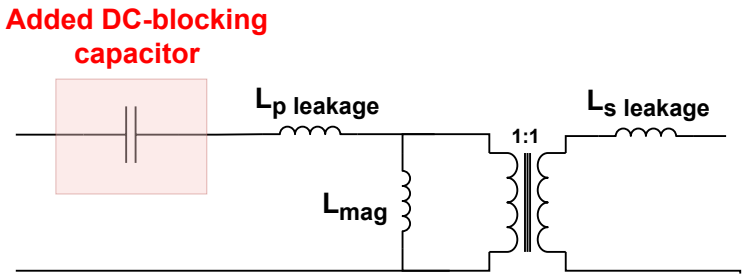

Figure 2.7: Schematic of implemented DC-blocking capacitor

Another passive way to prevent saturation is to include an air gap inside the transformer core magnetic path. When this is done, the relative permeability of the core is decreased which allows the transformer to withstand a higher DC magnetization without saturating. This however does not remove the DC flux component as the DC blocking capacitor would. The addition of an air gap also increases the peak value for the magnetizing current which would cause increased losses in switching and conduction [15].

Another way to passively prevent saturation is by operating the transformer with long dead-times between duty cycles, allowing the transformer's passive properties to dissipate the accumulated flux. However this method significantly increases conduction in both the diodes and the transistors. Increasing reverse recovery losses.

2.3.2 Active flux balancing methods

Active flux balancing is when the flux in the transformer is measured or estimated and a controller implements a control action to counteract the flux inside the transformer. This can be done by changing the voltage. In a PSFB-DAB converter, changing the voltage is done by making a slight change in the duty cycle on the primary, secondary or both sides of the converter to eliminate the DC bias over the transformer.

To implement this type of control, a flux measurement or saturation detection method is required to provide feedback to the controller. This allows the controller to determine when and to what extent the flux needs to be controlled.

The most direct method for measuring magnetic flux is to insert a flux sensor into the magnetic flux path and directly measure its value. However, this approach requires physical space within the flux path, which in most cases implies the use of a gapped core. Furthermore, the method must account for potential issues such as sensor saturation and temperature-induced measurement errors due to sensor heating.

In [11], a flux measurement method is proposed that involves the use of an auxiliary core, referred to as the "Magnetic Ear", which shares the magnetic path with the main core. This auxiliary core includes its own winding, allowing instantaneous detection of changes in its inductance. These inductance variations are highly sensitive to the instantaneous magnetization state of the main core, making them a reliable indicator of the core's magnetization [11].

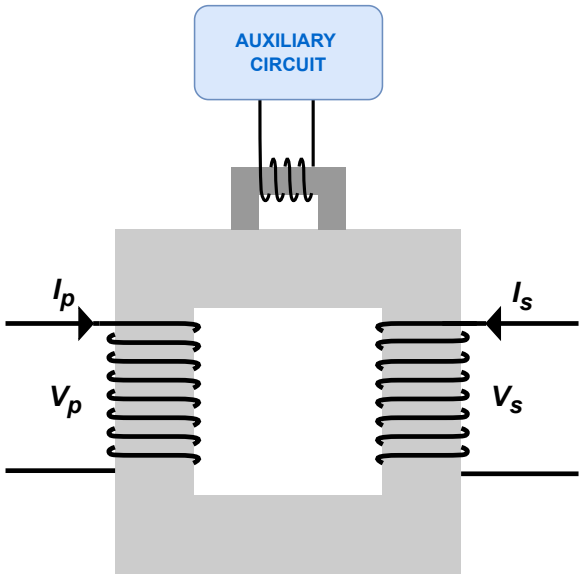

Figure 2.8: Simplified schematic of "Magnetic Ear"

This method however, has its drawbacks including the need to modify the transformer core's physical structure, as well as only being able to detect changes in inductance in cores where the permeability of the core continuously changes along the B-H curve. For example, in gaped cores where the B-H loop is linear until saturation, only saturation can be detected.

In cases where the transformer is wound and the primary and secondary windings are close enough to be placed next to each other, the flux can be measured using a Hall sensor between the windings [16]. This is illustrated in Figure 2.9.

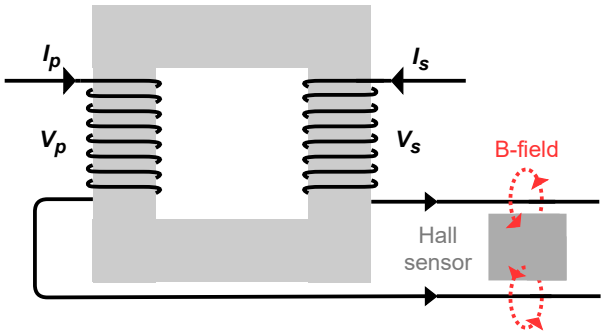

Figure 2.9: Simplified schematic of Hall sensor implementation in between windings

This method works if the turn ratio is unity or simple fraction, and the insulation requirements are not demanding. There are also flux saturation correction methods where saturation detection is used to implement a control action when core saturation characteristics are detected [17]. This however is not optimal since when the core reaches saturation it is already in an undesirable state that compromises the performance. This method also requires modification of the transformer structure as seen in [18].

Integrating the applied voltage to the transformer to obtain the flux is proposed in [19]. This could be used to detect the flux unbalance due to variations in the loading conditions of the converter. However, due to the need for integration, only changes in the flux can be detected. This results in steady-state errors remaining undetected. Figure 2.10 shows how this can be implemented with an RC-network integrator.

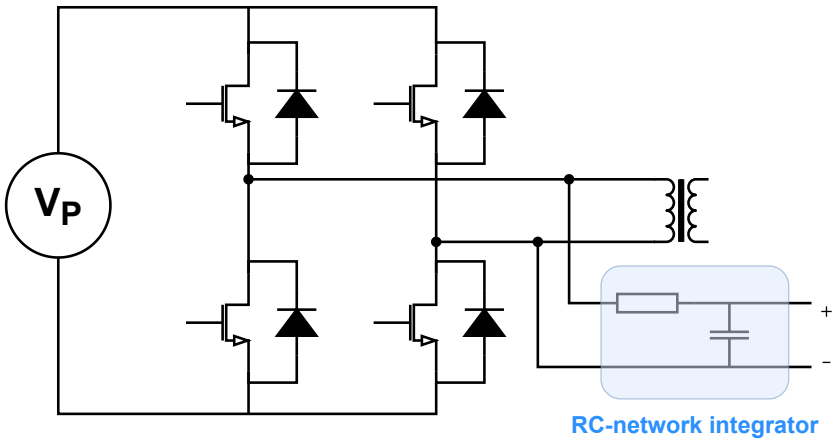

Figure 2.10: Schematic showing implementation of a RC-network integrator

Another method is to measure the magnetic current $i_m(t)$ which is directly related to the flux density in the core. Although this approach is more complex than estimating $i_m(t)$, through subtraction of the primary and secondary currents while

accounting for winding ratio as suggested in [19]. This approach instead requires non-invasive current measuring with relatively good accuracy to access the current to control.

2.3.3 Shunt current sensing

Shunt current sensing utilizes Ohm's law by inserting a resistor of a known value into the circuit. This resistor is then used to cause a voltage drop which is proportional to the current flowing in the circuit. The voltage over the resistor is then simply measured and dividing the measurement by the known resistance gives the current using Ohm's law. This same method can also be utilized without adding a dedicated shunt resistor, for instance by using an existing conduction element in the circuit such as a copper trace [20]. This method does not require any additional components inside the circuit which prevents additional power loss. However the resistance of a copper trace is very low which gives a very small voltage drop [20]. Which results in the need for additional amplification circuits to implement the control.

2.4 Softwares

In this section the software utilized during the thesis is introduced together with their respective usage areas.

2.4.1 Simulink

Simulink [21] is a simulation software that lets users create block diagram environments that translate to simulation models. The blocks can execute complex mathematical calculations without the requirement of additional code. Simulink offers pre-developed models of electrical components from the Simscape library such as transformers, MOSFETs and measuring equipment. Simulink also offers component models of both ideal and non-ideal characteristics which broadens the simulation possibilities and how the results correlate to real life operation [22].

2.4.2 LTspice

LTspice [23] is a simulation software where users can build electrical circuits and analyze different signals and measurements. SPICE stands for Simulation Program with Integrated Circuit Emphasis [24]. LTspice offers users circuit modeling possibilities with both ideal and specific component operation which makes it possible for users to design circuits with specific components to closer mimic real life operation. LTspice enables many different methods to analyze and verify simulation of electrical circuits, for example by performing frequency analysis and signal measurements [25].

2.4.3 Bode Analyzer Suite

Bode Analyzer Suite is a graphical user interface where the user can configure a Bode 100 to match their specific measuring requirements. The software offers both impedance and gain measurements for a large frequency range which enables thorough analysis of the connected component or circuit. In Bode Analyzer Suite the user can plot their measurements and analyze properties such as stability with the help of available cursors and mathematical tools [26].

2.5 Bode 100

The Bode 100 is a vector network analyzer and frequency response analyzer which can be used for complex impedance measurements and stability analysis of control circuits [27]. The bode 100 can also be used for modeling transformers and their parasitic elements, as well as measure leakage inductance of both the primary and secondary side of the transformer [28].

The Bode 100 has three ports, output, channel 1 and channel 2. The output channel sends out sine waves at different frequencies while channel 1 and channel 2 simultaneously measures the voltage. The software Bode Analyzer Suite uses the magnitude and phase ratio of these signals to calculate factors such as impedance, reflection and complex gain values for the test object [29].

2.6 Monte Carlo method

The Monte Carlo method is often used to asses the risk probability of an electrical system using a mathematical model [30]. The Monte Carlo method is based on statistics and in circuit analysis the tolerance for each component is taken into account. The basic methodology of Monte Carlo is that a sweep is made for the electrical circuit where different values within the tolerance range are used randomly for different components. This way, the results become random and a better overall result for the circuit can be achieved in contrast to only changing the value for one component within its tolerance range.

Monte Carlo can be used in SPICE simulations for circuit analysis and is a great tool to mathematically predict the characteristics of a circuit. This is very helpful in large scale PCB production as the risk of component value deviations become larger when more components are involved.

2.7 State-space model

A state-space model can be used to create a mathematical model of a linear time-invariant (LTI) system [31]. The state-space model of a system can be utilized for many things such as control analysis and controller design. If the relation between input and output of a continuous time dependent system can be written on the form

$$\begin{aligned} \dot{x}(t) &= Ax(t) + Bu(t) \qquad \text{(State equation)} \\ y(t) &= Cx(t) + Du(t) \qquad \text{(Output equation)} \end{aligned} \tag{2.1}$$

a state-space form of the system can be defined. In (2.1) $\dot{x}(t)$ represents the derivative of the state vector $x(t)$, $y(t)$ is the output vector and $u(t)$ is the control vector. A, B, C and D represent the state, input, output and feed through matrices respectively.

2.8 PI-control

The PI-controller is the most common control scheme used in industry today [32]. This is because of their effectivity for controlling various systems as well as their simplicity in implementation. These controllers can also be implemented without having to model the system mathematically. The controller consists of both a proportional and integral control term which together work to minimize the error signal

$$e(t) = X_{ref}(t) - X_{actual}(t) \tag{2.2}$$

where X_{ref} is the reference value and X_{actual} is the real value. The error is calculated as the difference between the reference and the real value. The proportional term takes the error signal $e(t)$ and multiplies it with the constant proportional gain K_p while the integral term integrates the error over time with the integral gain K_i [32]. The output of the controller $u(t)$ can then be determined as

$$u(t) = K_p e(t) + K_i \int_0^t e(\tau) d\tau \tag{2.3}$$

where the proportional term is responsible for the bulk of the change in the output. A low proportional gain will result in a too slow response but with a too high proportional gain the system can become unstable. The integral term is used to minimize steady-state errors, but it can also make the system more unstable and may cause oscillatory behaviors.

3

Case Setup

The simulation software Simulink was used together with Matlab to build the transformer model and controllers. Matlab was mainly used for deriving the state-space matrices, while Simulink was used to generate DAB converter switching signals, build the transformer model as well as to build the controllers for the flux and current control. The controllers were implemented to limit magnetizing current and prevent drifting between the primary and secondary currents. Evaluation of the control was performed and compared to testing on the real converter.

3.1 State-space model derivation

To build a state-space model, equations that express the state variables need to be defined. These equations can be derived from several different types of models but they essentially describe how the different parameters relate to each other in equation form. For the transformer in this thesis, the state-space equations were obtained from the magnetic equivalent circuit.

3.2 Transformer model

The simulation model developed in this thesis was developed using Simulink. A model of the full bridge converters had already been created and was provided by Aros Electronics AB. This model was used to provide voltage signals for the transformer simulation model.

Matlab was used to define the A, B, C and D matrices while the state-space Simulink block was used to implement the state-space model in the simulation model. Figure 3.1 shows how the voltage signals provided by the full bridge models are feed into the state-space block and used to calculate the primary and secondary currents. The magnetizing current is then calculated by taking the difference between the primary and secondary current.

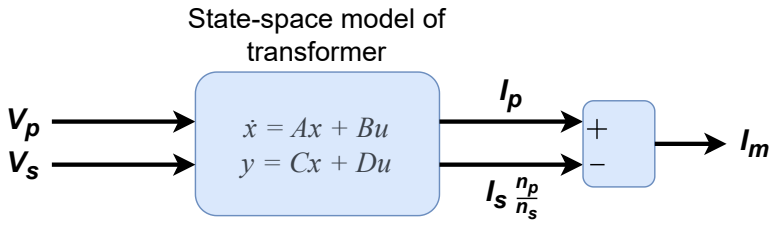

Figure 3.1: Transformer state-space model implementation in Simulink simulation

3.3 Transformer parameter measurements

Parameters such as the leakage and mutual inductance of the transformer were initially unknown. Because of this they had to be experimentally determined and measured on the hardware. The method used to do this originates from OMICRON's own transformer modeling instructions using a Bode 100 [28].

Firstly, the Bode 100 was calibrated using the inbuilt calibration function where an open circuit, short circuit and loaded test was performed. After the calibration was finished, the primary side winding resistance R_1, was measured. This was done through a One-Port measurement method where the output channel on the Bode 100 is connected to the primary side of the transformer as seen in Figure 3.2, while the secondary side of the transformer remains open-circuited.

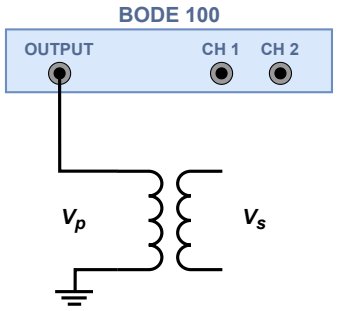

Figure 3.2: Measurement setup for primary leakage and magnetizing inductance

The Bode 100 was connected to a computer and controlled through the software Bode Analyzer Suite, where a frequency sweep and impedance analysis was conducted. The results of the frequency sweep showed the impedance as a function of frequency, where R_1 was measured at a frequency value where the trace was at a stable value.

To measure the leakage and magnetizing inductance of the primary side, another One-Port measurement was preformed. For this measurement the sum of the leakage and magnetizing inductance for different frequencies was measured. The measured inductance value decreases for higher frequencies since the core resistance also de-

creases for high frequencies, therefore the measured inductance should be read at a frequency where the measurement contains less noise and before the measurement values start to drift. The measured value in this One-Port measurement is called L_1.

Since the values of the magnetizing inductance and the leakage inductance need to be defined separately for the state-space model, a gain-measurement was conducted to retrieve their independent values. The setup for this measurement can be seen in Figure 3.3.

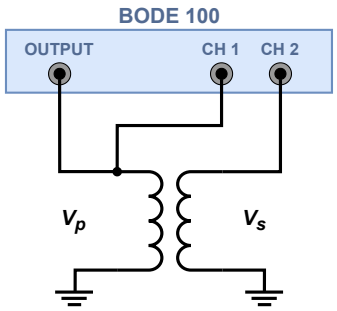

Figure 3.3: Measurement setup for primary magnetizing inductance

For this measurement method, the gain G, was measured in a frequency sweep. The gain at the same frequency used to decide L_1 in the previous One-Port measurement was read and used in

$$G = \frac{\omega L_m}{\sqrt{R_1^2 + (\omega L_1)^2}} \frac{1}{a} \tag{3.1}$$

where ω is the angular frequency at the same frequency as L_1 was measured. The variable a is the turn ratio and L_m is the magnetizing inductance. L_m was calculated from (3.1) as

$$L_m = \frac{G}{\omega} \sqrt{R_1^2 + (\omega L_1)^2} \tag{3.2}$$

when the turn ratio of the transformer was $1:1$. From this the primary side leakage inductance L_{lp}, was finally calculated as

$$L_{lp} = L_1 - L_m \tag{3.3}$$

The same procedure was used to calculate the secondary side leakage inductance. The calculated values were fed into the state-space model in Simulink to get a transformer model that was more realistic to the real operational case.

To verify the measurements an open circuit and a short circuit measurement was also conducted and used to calculate the inductances. This calculation method was considerd not as accurate but was used to verify the magnitude of the previous measurement.

3.4 Control implementation in Simulink

Two PI-Controllers were implemented into the Simulink model, one flux balancing controller used for bringing the average value for the magnetizing current to zero and one DC offset controller used for bringing the average value of the primary current to zero. For simulation, discrete PI controllers with a bandwidth of 5000 Hz were used to mimic the limited bandwidth of the control loop in the target's software. Theoretically controllers with only proportional gain (P) controllers might suffice for the application, however they would require very high measurement resolution which is why PI controllers were implemented instead.

3.4.1 Flux balancing controller

The flux balancing controller was implemented to control the average value of the magnetizing current to zero to prevent saturation of the transformer core. Figure 3.4 shows a simplified feedback system of the flux balancing control.

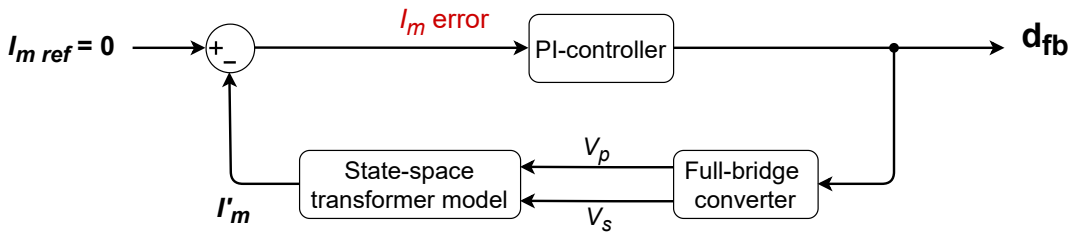

Figure 3.4: Feedback system of flux balancing control

The average value of the magnetizing current was calculated by passing the magnetizing current signal I_m, through a low pass filter. The average value of the magnetizing current, I'_m, was then compared with the reference value of the controller $I_{m,ref} = 0$, to calculate the error. The error was then fed into the PI controller to calculate the duty cycle signal that needs to be added to the switching duty cycles to reach the reference value and a steady state. The duty cycle output signal from the PI controller is added to both the primary and secondary side duty cycles. In this way the voltage could be adjusted so that the magnetizing current would reach the desired value.

3.4.2 DC offset controller

After the implementation of the flux balancing controller. The DC offset controller was added to prevent DC offset from forming in the primary or secondary side currents. A DC offset in either current tend to result in the equal offset in the other current. This could cause the currents to push the signal outside the hardware's limited measurement range, potentially leading to component damage due to excessively high currents. The average value of the primary current I'_p, was controlled to reach a steady state of zero. Figure 3.5 shows a simplified feedback system of the DC offset controller.

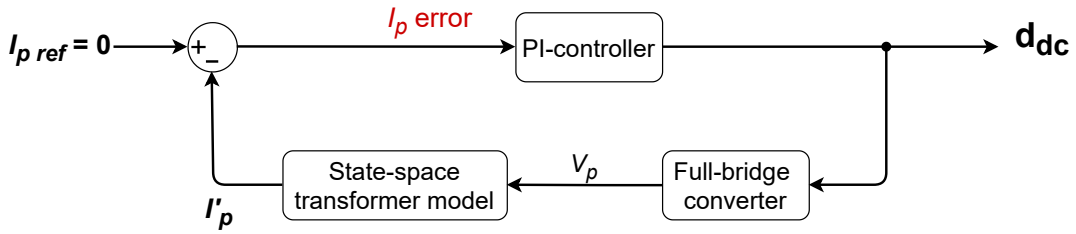

Figure 3.5: Feedback system of DC offset control

The feedback works similarly to the flux balancing controller, except that I'_p is controlled to zero instead of the magnetizing current. The calculated error is than fed into the PI controller and the output duty cycle is only added to the primary side duty cycle signals. This control system brings I'_p to zero. Because of the characteristics of the flux balancing controller, the secondary side current is pushed to follow the primary current. In this way the average current of both the primary and secondary side are controlled to 0 and by combining both controllers, the drifting between the current waveforms is eliminated.

3.4.3 Proposed hybrid control

As previously mentioned, in theory the flux in the transformer can be estimated through integrating the applied voltage to the transformer. Due to the integration this method can not detect steady state errors which prevents it from being used. However, using this flux detection method together with the already implemented current measurement could create a hybrid control scheme. That in theory could outperform the already existing implementation. This proposed method is purely theoretical and is only practical if the voltage measurement has a lot higher bandwidth than the current measurement. In general, the current measurement requires really small voltage signals to be measured if shunt measurements are being used which could be more challenging compared to the voltage measurements. This hybrid control approach was implemented in simulation and investigated compared to the previously mentioned implementation. A simplified model of the implementation can be seen in Figure 3.6.

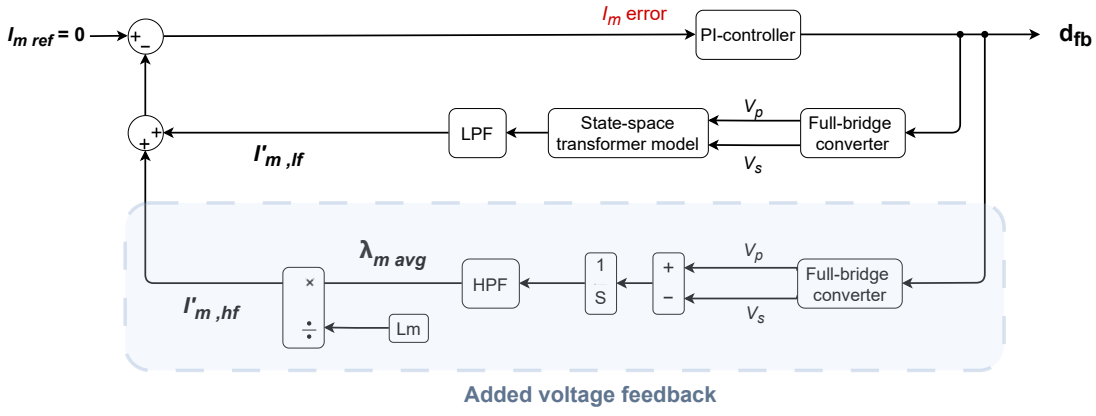

Figure 3.6: Feedback system of hybrid control

The voltage measurement method was implemented in a way that it complements the current measurements by feeding the flux balancing controller the high frequency part that is estimated from the measured voltage. Basically trying to artificially increase the bandwidth of the current measurement. This allows for faster feedback results in a faster controller with better disturbance rejection at a wider range of frequencies. This is implemented by high pass filtering the signal from the voltage measurements while the current measurement signal is low pass filtered. The filters have non-overlapping cutoff frequencies. This then adds to the error of the flux balancing controller resulting in a quicker action to the system dynamics as compared to only the current measurements.

3.5 Three variable sweep setup

A three-variable sweep was performed to study how phase shift ϕ, primary voltage V_p, and secondary voltage V_s influence controller behavior and the resulting plant gains used for tuning. Additionally, I'_m was measured to evaluate control performance.

The variables were swept between their max and minimum values with appropriate sectioning between each step. Table 3.1 shows the swept parameter values for each variable.

Table 3.1: Three variable sweep parameter values

V_p [V]	550	650	750	850	
V_s [V]	550	650	750	850	
Phase-shift [ϕ]	$-90°$	$-45°$	$0°$	$45°$	$90°$

The sweep was performed using a custom script that launches 16 Simulink simulations in parallel, with each simulation running on a separate processor thread. The process is initiated by a batch file that creates 16 individual MATLAB instances each responsible for handling a unique voltage combination.

Each MATLAB instance runs one Simulink simulation for its assigned voltage combination and phase shift, resulting in 5 simulations per instance. This setup yields a total of 80 simulations. This approach was necessary due to the large number of simulations combined with the need for extremely high accuracy, which led to unreasonably long simulation times.

The data was then down sampled to reduce storage requirements and simplify handling before being saved and analyzed. The simulation was run with all tuned controllers active and a 3V step was added to the secondary side voltage at 0.0075s. This data was then analyzed to calculate the slopes and corresponding gains for the different operating conditions, which were later used to tune the converters.

3.6 Tuning methodology

The PI controllers were tuned to achieve optimal control parameters using MATLAB's pidtune() function, which designs controllers based on linear time-invariant (LTI) models. However, linearizing the system's PWM modulation to obtain an LTI model proved challenging. To address this, an alternative approach was taken by linearizing the current as a function of the duty cycle, resulting in an equivalent model. This method is justified by the assumption that the output voltage magnitude is proportional to the converter's duty cycle. Within the operating interval, this relationship simplifies the system, allowing the transition to be modeled as a gain.

Several different tunings were also performed for varying magnetizing inductances of the transformer. They were then tested and the best tuning suited for the whole range was chosen. This was done to ensure that the controller could handle inductance values ranging from 1 mH to 3 mH, as the transformer's magnetizing inductance can vary within this range. This is due to the system's sensitivity to air gaps, where surface imperfections can introduce small gaps that significantly affect the magnetizing inductance. Additionally, the magnetic material itself has a wide tolerance range of about 30%, which must be accounted for in the controller design.

3.6.1 Flux balancing controller tuning

The gain for the equivalent system was calculated by studying the magnetizing current for the additional duty cycles contributed by the converter. Ranging between 0 and 0.05 which is the positive side of the operating range of the output of the controller. The negative side of the operating interval was verified to have the same response and was because of this neglected during gain estimations. For these simulations all controllers were disabled. The gradient of the current response was calculated for each duty cycle value and plotted. A linear regression model was used to estimate a linear relationship between the gradient values previously calculated. The slope of the regression line, representing the rate of current change per duty cycle, was then used in the linearized version of the model as the gain. The linearized model for the flux balancing control system can be seen in Figure 3.7.

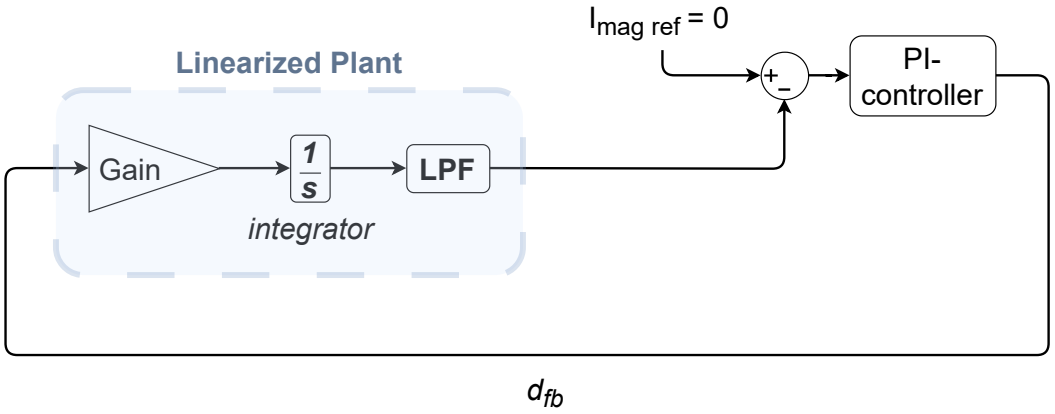

Figure 3.7: Linearized model of flux balancing control system

The model simulates the relationship between the control signal and output voltage by multiplying the converter's control signal by a gain factor, reflecting the proportional dependence of voltage on duty cycle. The resulting difference is integrated over time and low pass filtered to model the additional delay introduced by the filter. This integrated voltage difference represents the magnetic flux, which is directly proportional to the current being controlled I_m.

To achieve a similar step in the linearized model as the original model the applied step also had to be adjusted. This was done to produce a step of equal magnitude as in the original model. The size of the step was approximated to

$$V_{step} = \frac{\frac{1}{V_p}G}{2} \tag{3.4}$$

where G represents the previously calculated gain and V_{step} the magnitude of the step applied to the system. The calculated voltage step was then validated against the original simulation model and slightly adjusted to achieve a step response that matched the behavior of the original model.

Once the equivalent system was constructed and verified to have the same step response as the original system, it was rewritten as a transfer function and used to tune the controller analytically. The tuning for the flux balancing controller was set to achieve the quickest control possible with a phase margin of $\theta = 60°$.

3.6.2 DC offset controller tuning

Once the flux balancing controller had been tuned, the DC offset controller could also be adjusted. To determine the gain for the equivalent system, the primary-side current was simulated with the tuned flux balancing controller active. Additional duty cycles between $0 - 0.025$ were applied, corresponding to the positive side of the converter's operating range. As with the flux controller, the negative part of the operating interval was verified to produce the same response and was therefore

neglected. The same procedure used for the flux controller was applied to determine the slope of the primary side current. A regression line was then plotted, and its slope was used as the gain. The equivalent step was then calculated according to (3.4).

After verifying that the model exhibited the same step response as the original system, the DC offset controller was tuned to be ten times slower than the flux balancing controller, with a phase margin of $\theta = 60°$. This tuning approach was chosen to minimize the DC offset controller's interference with the flux balancing controller, while still ensuring a response fast enough to effectively control the current.

3.6.3 Hybrid control tuning

For the implementation of the hybrid control, which incorporates a second measurement source with higher bandwidth into the existing flux balancing controller, the previously established tuning parameters were used.

3.7 Sensitivity analysis

To ensure reliable current measurement in the presence of component tolerances and thermal variations, a structured tolerance analysis was carried out using LTspice simulations. The objective was to quantify the impact of component variations on measurement accuracy. The approach included sensitivity analysis, extreme-value evaluation, and Monte Carlo simulations conducted at two different temperatures. This includes the nominal temperature of 25 °C and the maximum operating temperature of 100 °C.

3.7.1 Component sweep

To conduct a sensitivity analysis, a LTspice model was constructed and modeled after the amplification circuits provided by Aros electronics. Since not all components used in the amplification circuits were available in the LTspice library, models from the manufacturers websites were manually converted from standard SPICE models into LTspice models. For the IC circuits, frequency analysis was used to verify that the gains aligned with the datasheet specifications.

Initially an ideal case was set up with a nominal temperature of 25 °C and ideal component values. The output peak to peak voltage as well as the average output voltage was measured for this case and used as a reference for the following simulations.

Following this, a sensitivity analysis of the amplification circuitry was conducted to better understand which components affect the amplification the most. Each component in the LTspice simulation model was individually varied by ±10% of its nominal value, and the resulting average output voltage was measured. Although a

10% variation is larger than the tolerance ratings of the components used in the actual circuit, it was intentionally chosen to clearly highlight which components have the greatest impact on output voltage. It is also important to consider the threshold voltages of the different ICs used, but during the component sweep these remained inside of their operating range.

To assess the influence of component tolerances on amplification, an initial analysis was carried out by setting the six most critical components to the extreme ends of their allowable tolerance ranges. This approach was used to estimate the maximum potential amplification error. However, this method does not accurately represent typical operating conditions, as component values generally vary randomly, and some deviations may partially cancel each other out. To better reflect these realistic variations, a Monte Carlo analysis was also performed.

3.7.2 Monte Carlo analysis

To model realistic temperature and tolerance variation across the components, Monte Carlo simulations were conducted in LTspice, with all component values randomly varied within their specified tolerance ranges over 500 iterations. The changing resistor values were calculated as

$$R = R_{MC}(1 + T_{coeff}(T - T_{nom})) \tag{3.5}$$

where R represents the resulting resistance in the simulation, R_{MC} is the resistance decided using the Monte Carlo method, T_{coeff} is the temperature coefficient, T is the simulation temperature and T_{nom} is the nominal temperature. T_{nom}, T_{coeff}, resistance at nominal temperature as well as the resistance tolerance values were all found in the datasheet for each resistor in the circuit.

Since capacitors generally show a non-linear relationship between temperature and capacitance, temperature-specific capacitance values were manually added to each capacitor in the simulation model. These values were taken from the manufacturers websites.

Simulations were performed at two temperature points: 25 °C (nominal) and 100 °C (the estimated maximum operating temperature of the converter). For each iteration, the gain and average output voltage were calculated and statistically analyzed to characterize typical variation and the influence of elevated temperature. These simulations were compared to the previously simulated ideal case.

To isolate the effects of temperature from component tolerance, an additional simulation was performed using ideal component values at 100 °C. Temperature-dependent component characteristics were sourced from manufacturer data sheets and applied to the LTspice model. This allowed direct comparison of temperature-induced gain shifts without the confounding influence of component variability.

3.7.3 Measurement error estimation

The total gain deviation was defined by combining the maximum observed variation due to component tolerances with the gain shift caused by temperature. This total deviation was then used to estimate the resulting input voltage measurement error. Since the measurement is taken across a trace with known resistance, the voltage error was converted into a corresponding current estimation error.

In the implemented system, both primary and secondary current measurement signals undergo initial calibration at startup. As a result, any gain error present at that time is canceled out by the calibration process. Since component variation is present in the initial stage, this is effectively cancels out during calibration. As a result, only deviations caused by drifting temperatures remain relevant during runtime. The worst-case scenario was defined as a condition where one current path remains at 25 °C, while the other rises to 100 °C, creating an imbalance that represents the maximum expected error in magnetizing current estimation.

3.8 Test cases

In this section the different cases used to test the functionality of the controllers in simulation is presented. To evaluate the efficiency of the controller, test cases for simulation was setup and used to test the controllers performance.

3.8.1 Case 0

Initially a base case was used to show how the Simulink model performs with all controllers turned off. Utilizing the base operation condition of 1 : 1 voltage ratio with a phase shift of 0°. 850 V was used on both the primary and secondary side. In this case a 1 V step was applied at 7.5 ms.

3.8.2 Case 1

Case 1 was designed to evaluate the performance of the flux and DC offset controllers, along with the implementation of the dead-time effect. These were tested in the Simulink model using a sequence of voltage steps applied to the secondary side of the transformer. The applied steps are specified in Table 3.2.

Table 3.2: Actions in case 1

Time (ms)	**Action**
7.5	Apply step of 0.5 V
15	Remove step of 0.5 V
25	Apply step of 2.0 V

To evaluate the controllers without interference from other variables, the phase shift was fixed at 0° and the voltage ratio was set to 1:1.

3.8.3 Case 2

Case 2 is designed to evaluate the systems characteristics during a worst-case scenario. The base of case 2 is identical to case 1, apart from that the worst-case combination of voltage ratio and phase shift is used in the model. The worst-case combination of thee voltage ratio and phase shift is defined in the three variable sweep as a primary voltage of 850 V, a secondary voltage of 550 V together with a phase shift of $-90°$. The steps defined in Table 3.2 are used to evaluate the model and easily analyze how the worst-case variables affect the system.

3.8.4 Case 3

Case 3 was used to test the maximum step the controller could handle before saturating the transformer or becoming unstable. This was done by gradually increasing the magnitude of the step until either the controller reached instability or the magnitude of the magnetizing current reached the saturation threshold. This case utilizes both controllers together with the dead-time effect implementation, as well as the three variable sweep worst-case scenario.

4

Analysis

4.1 Transformer model

A state-space model of the transformer was chosen because of its simplicity together with its ability to provide a framework for understanding system dynamics, controllability and providing observability. State-space models also provide very quick simulation time compared to existing transformer models in programs like Simulink which greatly improved our ability to quickly test and implement controllers.

4.1.1 Derivation of magnetic equivalent circuit

The magnetic equivalent circuit was derived from the base model of the transformer seen in Figure 4.1. In this model I_p and I_s represent the primary and secondary side currents. ϕ_{Lp} and ϕ_{Ls} are the primary and secondary side leakage fluxes. ϕ_m is the magnetizing flux and n_p together with n_s represent the number of turns of the primary and secondary side windings.

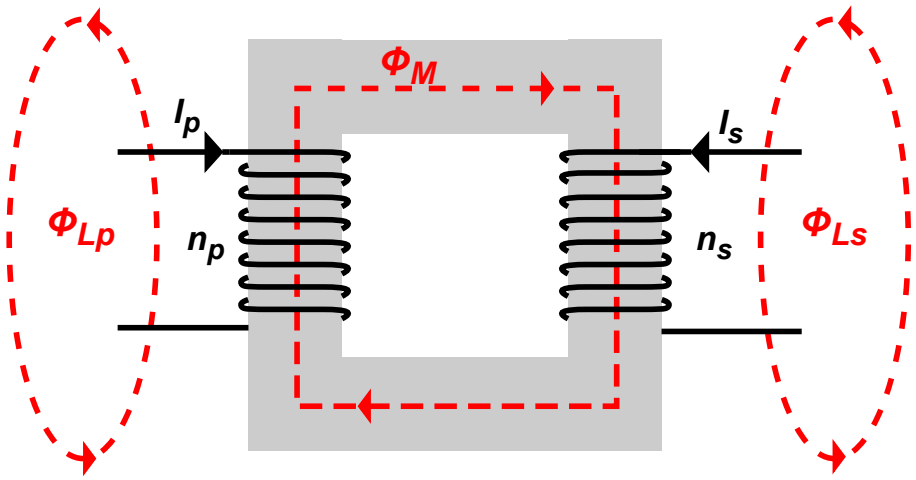

Figure 4.1: Transformer flux model

Figure 4.2 shows the magnetic equivalent circuit derived from the model in Figure 4.1. In the equivalent model, R_m represents the magnetizing reluctance. R_{Lp} and

R_{Ls} represent the leakage reluctance on the primary and secondary side. $\mathcal{F}_p$ and $\mathcal{F}_s$ represent the primary and secondary side magnetomotive force (MMF). ϕ_p and ϕ_s represent the total primary and secondary side flux.

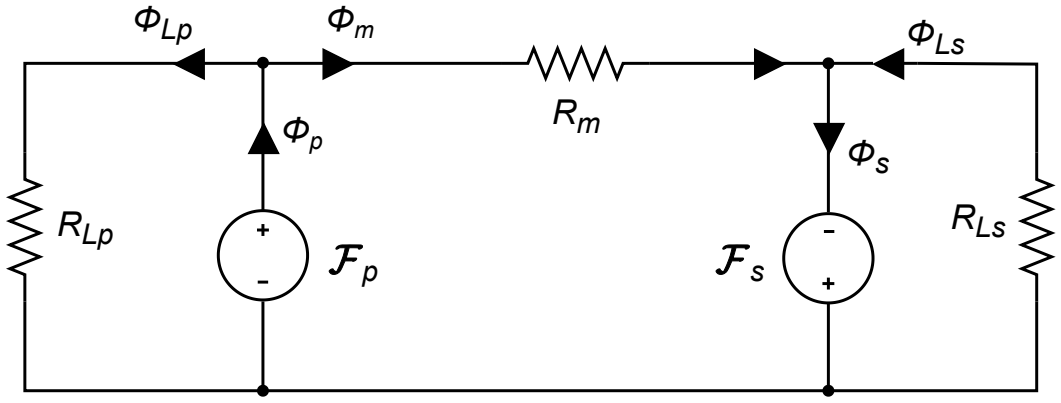

Figure 4.2: Equivalent magnetic circuit of the transformer

From the magnetic equivalent model several equations can be derived. The primary and secondary side leakage flux can be calculated as

$$\phi_{Lp} = \frac{\mathcal{F}_p}{R_{Lp}} \tag{4.1}$$

$$\phi_{Ls} = \frac{\mathcal{F}_s}{R_{Ls}} \tag{4.2}$$

where ϕ_{Lp} and ϕ_{Ls} are derived from Kirchhoff's voltage law (KVL). Furthermore the relationship between the different flux paths can be described as

$$\phi_p - \phi_{Lp} - \phi_m = 0 \tag{4.3}$$

$$\phi_s - \phi_{Ls} - \phi_m = 0 \tag{4.4}$$

by using Kirchhoff's current law (KCL), which explains the relationship between the sum of different currents in one node. From KVL in the inner middle loop of the equivalent model, ϕ_m can be expressed as

$$\mathcal{F}_p + \mathcal{F}_s - \phi_m R_m = 0 \rightarrow \phi_m = \frac{\mathcal{F}_p + \mathcal{F}_s}{R_m} \tag{4.5}$$

Ohm's law also gives that

$$\mathcal{F}_p = n_s I_p \tag{4.6}$$

$$\mathcal{F}_s = n_s I_s \tag{4.7}$$

and explains the relation between primary and secondary side MMF, number of turns and current.

Figure 4.3 shows a simplified electrical equivalent model of the transformer that has been derived from the model in Figure 4.2. In this model U_p and U_s represent the

primary and secondary voltage. L_{Lp} and L_{Ls} represent the leakage inductance of the primary and secondary side while L_{mp} represents the magnetizing inductance seen from the primary side. The currents i_p, i_s and i_m visualize the primary, secondary and magnetizing currents respectively.

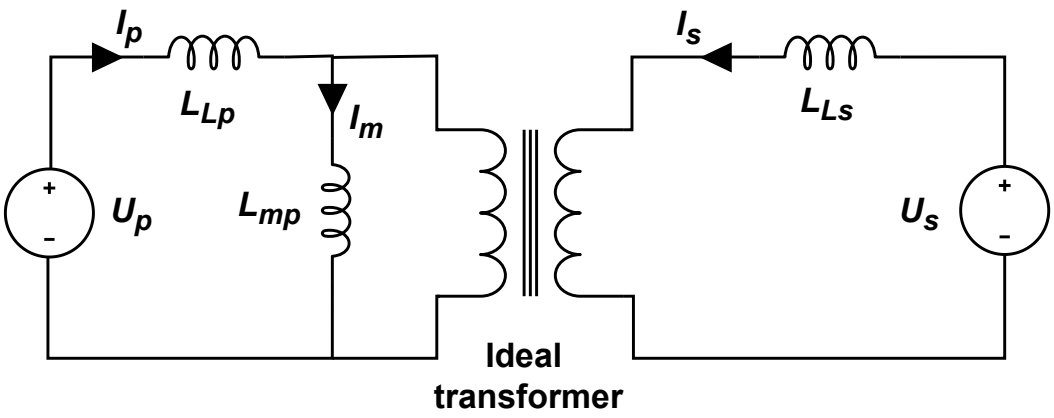

Figure 4.3: Simplified electrical equivalent model of the transformer

By combining equations derived from the magnetic equivalent model and the electrical equivalent model seen in Figure 4.3, together with Faraday's law of electromagnetic induction, the primary side voltage can be derived as

$$U_p = n_p \frac{d\phi_p}{dt} \tag{4.8}$$

inserting (4.3) in to the expression gives

$$U_p = n_p \frac{d}{dt}(\phi_{Lp} + \phi_m) \tag{4.9}$$

then replacing the fluxes with (4.1) and (4.5) gives

$$U_p = n_p \frac{d}{dt}\left(\frac{\mathcal{F}_p}{R_{Lp}} + \frac{\mathcal{F}_p + \mathcal{F}_s}{R_m}\right) \tag{4.10}$$

and finally inserting (4.6) and (4.7) into this and continuing to simplify the expression gives

$$\begin{aligned} U_p &= n_p \frac{d}{dt}\left(\frac{n_p i_p}{R_{Lp}} + \frac{n_p i_p + n_s i_s}{R_m}\right) \\ &= \underbrace{\frac{n_p^2}{R_{Lp}}}_{L_{Lp}} \frac{di_p}{dt} + \underbrace{\frac{n_p^2}{R_m}}_{L_{mp}} \frac{di_p}{dt} + \underbrace{\frac{n_p n_s}{R_m}}_{M} \frac{di_s}{dt} \\ &= \underbrace{(L_{Lp} + L_{mp})}_{L_{11}} \frac{di_p}{dt} + \underbrace{M}_{L_{12}} \frac{di_s}{dt} \end{aligned} \tag{4.11}$$

where M is the mutual inductance which also can be written as L_{12}. L_{11} is the self inductance of the primary side. The same derivation can be made for the secondary side voltage resulting in

$$\begin{aligned} U_s &= n_s \frac{d\phi_s}{dt} \underset{\text{eq. (4.4)}}{=} n_s \frac{d}{dt}(\phi_{Ls} + \phi_m) \\ &\underset{\text{eq.(4.2) and (4.5)}}{=} n_s \frac{d}{dt}\left(\frac{\mathcal{F}_p + \mathcal{F}_s}{R_m} + \frac{\mathcal{F}_s}{R_{Ls}}\right) \\ &\underset{\text{eq.(4.6) and (4.7)}}{=} n_s \frac{d}{dt}\left(\frac{n_p i_p + n_s i_s}{R_m} + \frac{n_s i_s}{R_{Ls}}\right) \\ &= \underbrace{\frac{n_s n_p}{R_m}}_{M} \frac{di_p}{dt} + \underbrace{\frac{n_s^2}{R_{Ls}}}_{L_{Ls}} \frac{di_s}{dt} + \underbrace{\frac{n_s^2}{R_m}}_{L_{ms}} \frac{di_s}{dt} \\ &= \underbrace{M}_{L_{21}} \frac{di_p}{dt} + \underbrace{(L_{Ls} + L_{ms})}_{L_{22}} \frac{di_s}{dt} \end{aligned} \tag{4.12}$$

where L_{ms} is the magnetizing inductance seen from the secondary side, L_{21} is equal to the mutual inductance M and L_{22} is the self inductance of the secondary side.

To simplify the calculation of the magnetizing current, i_s is expressed as a current from the view of the primary side by taking the winding ratio into account. i_m can now be written as

$$i_m = i_p + \frac{n_p}{n_s} i_s \tag{4.13}$$

according to KCL. The derived equations can now be used to define the state-space model of the transformer.

4.1.2 Resulting state-space model

To derive the A, B, C and D matrices for the state-space model as seen in (2.1), the equations from section 4.1.1 were utilized. First the voltage equations for the primary and secondary voltages were written in matrix form according to (4.8) and (4.12). The differential equations and output equations were then arranged in the standard state-space form. From the matrix equations

$$\begin{aligned} \begin{bmatrix} U_p \\ U_s \end{bmatrix} &= \begin{bmatrix} L_{11} & L_{12} \\ L_{21} & L_{22} \end{bmatrix} \frac{d}{dt} \begin{bmatrix} i_p & i_s \end{bmatrix} \leftrightarrow \\ \frac{d}{dt} \begin{bmatrix} i_p \\ i_s \end{bmatrix} &= \underbrace{\begin{bmatrix} 0 & 0 \\ 0 & 0 \end{bmatrix}}_{A} \begin{bmatrix} i_p \\ i_s \end{bmatrix} + \underbrace{\begin{bmatrix} L_{11} & L_{12} \\ L_{21} & L_{22} \end{bmatrix}^{-1}}_{B} \begin{bmatrix} U_p \\ U_s \end{bmatrix} \end{aligned} \tag{4.14}$$

the A and B matrices could be identified. Equation (4.13) was then written in matrix form as

$$i_m = \underbrace{\begin{bmatrix} 1 & \frac{n_p}{n_s} \end{bmatrix}}_{C} \begin{bmatrix} i_p \\ i_s \end{bmatrix} + \underbrace{\begin{bmatrix} 0 & 0 \end{bmatrix}}_{D} \begin{bmatrix} U_p \\ U_s \end{bmatrix} \tag{4.15}$$

which helps define the C and D matrices. From this, the A, B, C and D matrices are found to be

$$A = \begin{bmatrix} 0 & 0 \\ 0 & 0 \end{bmatrix}$$

$$B = \begin{bmatrix} L_{11} & L_{12} \\ L_{21} & L_{22} \end{bmatrix}$$

$$C = \begin{bmatrix} 1 & \frac{n_p}{n_s} \end{bmatrix}$$

$$D = \begin{bmatrix} 0 & 0 \end{bmatrix}$$

The state-space model of the transformer accurately models the inductances and the behavior of the magnetizing and leakage currents. However, it does not include any resistance modeling and therefore completely neglects parasitic resistances. As a result, certain simulation results deviate from real hardware behavior. Specifically, the primary and secondary side currents can grow to unrealistically large values in simulation, as they are not limited by the inherent winding resistances that exist in the physical transformer.

4.2 Transformer inductances

The primary winding resistance R_1, was determined with a 4 point Kelvin method using a low resistance ohm meter, measuring a resistance value of $R_1 = 19.407\text{m}\Omega$. To characterize the transformer's leakage and magnetizing inductance, a Bode 100 was utilized. A One-Port measurement was conducted to determine the combined inductance of the leakage and magnetizing components L_1. The resulting impedance plot is shown in Figure 4.4.

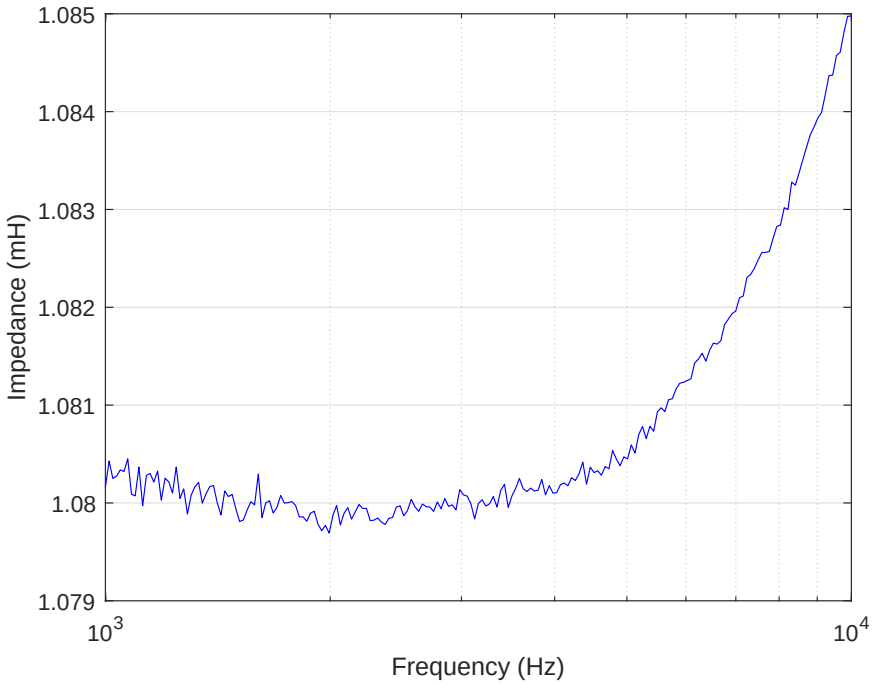

Figure 4.4: One-Port measurement results showing leakage and magnetizing inductance

At a frequency of 1kHz, the impedance of L_1 was measured to be 1.08198mH. For the gain measurement described in Figure 3.3, a vector network analysis was performed. The results for this measurement can be seen in Figure 4.5.

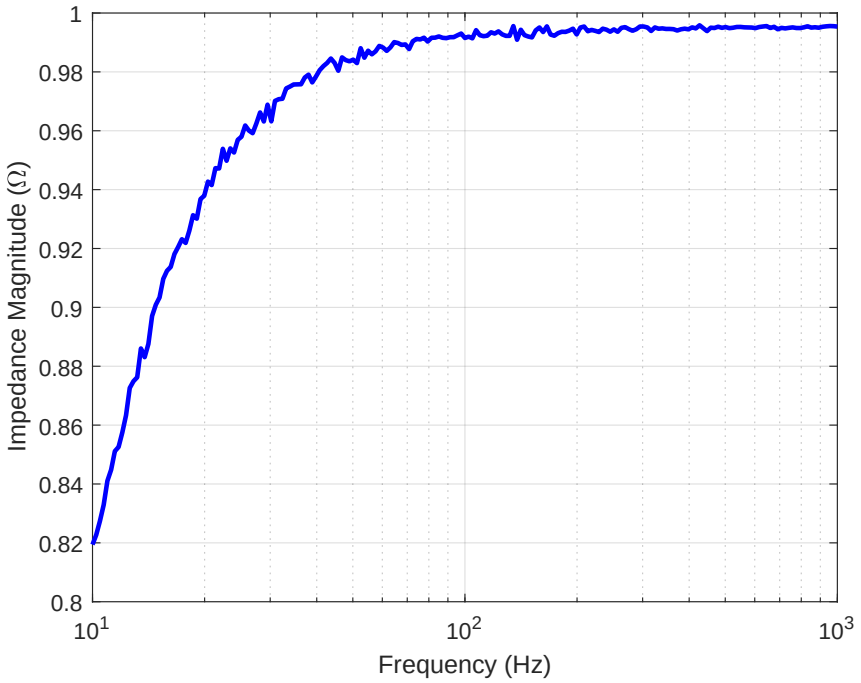

Figure 4.5: Gain measurement results

The gain, expressed as impedance magnitude on the Y-axis, was measured to be 0.99599mΩ at 100kHz. From this, the magnetizing inductance L_m, was calculated using (3.2) as

$$L_m = \frac{0.99599}{1000 \cdot 2 \cdot \pi}\sqrt{0.019407^2 + (1000 \cdot 2 \cdot \pi 1.08198)^2} = 1.07712\text{mH} \tag{4.16}$$

The leakage inductance of the primary side L_{l1} could then be calculated as

$$L_{l1} = 1.08198\text{mH} - 1.07712\text{mH} = 4.42\mu\text{H} \tag{4.17}$$

These inductance values were later implemented in the state-space model of the transformer in Simulink.

To verify the accuracy of the measured values, short-circuit and open-circuit tests were also performed. The results were used to calculate the magnetizing and leakage inductance's and confirmed that the measured magnitudes were within a reasonable range of expected values.

4.3 Three variable sweep

A three-variable sweep was used to determine the system gains needed for tuning the controllers. By applying a step input with the target controller disabled, the rate of change of the current slope could be observed under different converter voltages and phase shifts. This process was repeated for all combinations of the system variables. The resulting regression slopes were then combined, and the final regression line was used to define the plant gains for controller tuning. This plant can be seen in Figure 3.7.

With the controllers enabled, the three-variable sweep was repeated. By analyzing the magnetizing current, a worst-case operating condition could be identified. The peak value of I'_m was extracted for each simulation and was plotted in a 3D scatter plot to visualize the worst case with the largest peak. Figure 4.6 shows the results of the peak I'_m, for each simulation run. The largest peaks are colored in yellow while the smallest peaks are colored in dark blue.

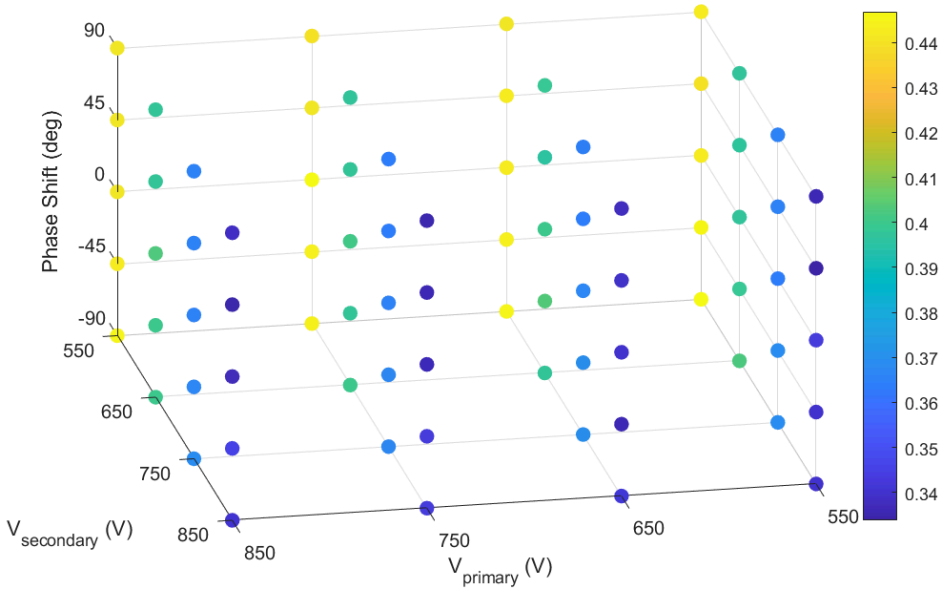

Figure 4.6: 3D scatter plot of 3 variable sweep results

The results indicate that the largest I'_m peaks occur when the primary voltage is at its lowest value, 550 V. This is because the step voltage is applied on the secondary side, and at lower primary voltages, this step represents a proportionally larger disturbance. The highest simulated I'_m peak was 0.4468 A.

Although variations in primary voltage and phase shift result in small differences that are difficult to distinguish in the plot, the data shows that higher primary voltages and the resulting larger voltage differences across the transformer tend to produce higher magnetizing currents. This occurs because the voltage step is applied to the secondary side of the transformer. If the secondary voltage is smaller, the same voltage step appears relatively larger by comparison. Additionally, for each voltage combination, phase shifts of higher magnitude, particularly negative ones, were associated with slightly higher I'_m. This observation contradicts the earlier assumption that the controller would respond symmetrically to both positive and negative phase shifts. However, the differences are minimal and are most likely due to sampling artifacts or variations in data processing. From this, the worst case scenario was defined as when the primary voltage was 850 V, the secondary voltage was 550 V, and the phase shift was $-90°$.

4.4 Frequency response analysis of controllers

In this section the results from the PI tuning of the two converters together with their respective stability analysis is shown.

4.4.1 Open loop frequency response

After tuning the flux balancing controller, the PI values were optimized to

$$K_P = 0.0040 \qquad K_I = 2.5943 \tag{4.18}$$

for the open loop transfer function of

$$\frac{3152.239s + 2044086.8}{0.0001061s^3 + s^2} \tag{4.19}$$

Where K_P is the proportional gain and K_I the integral gain of the controller. After applying these variables in the flux balancing controller the system's stability could be analyzed. A Bode analysis was mainly used as the foundation for the stability evaluation. Figure 4.7 shows a Bode plot of the open loop system for the flux balancing controller.

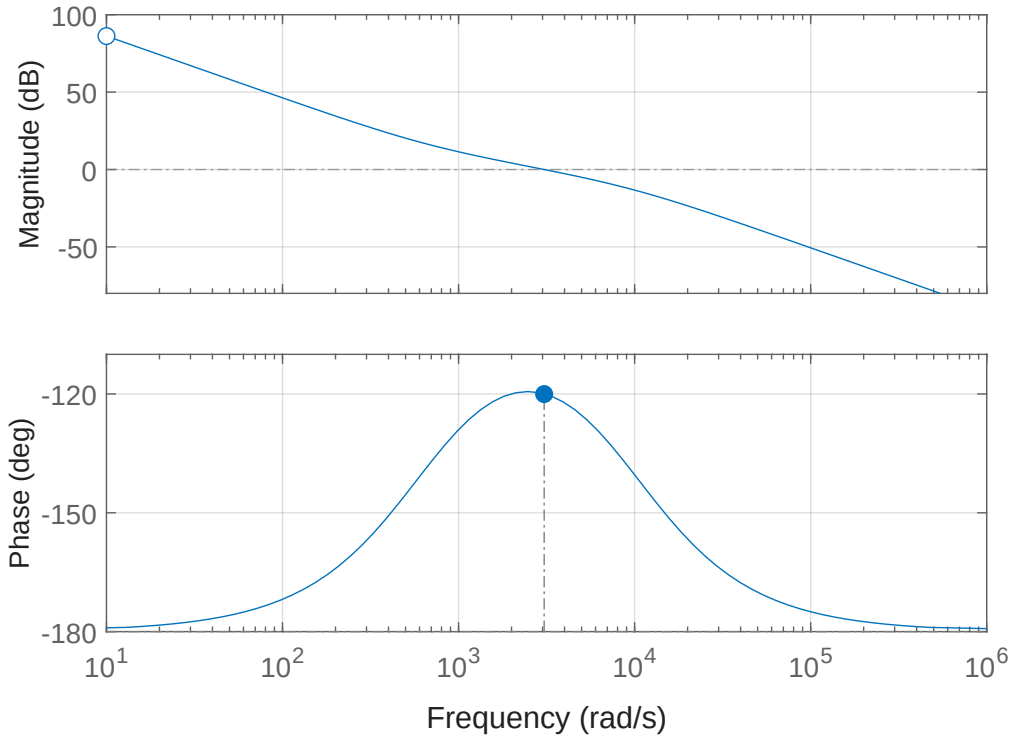

Figure 4.7: Bode plot of the open loop system for the flux balancing controller

It can be observed that the gain margin (Gm) for the open loop system is infinite. This is caused by the system never crossing the $-180°$ for the phase plot. This suggests that the system is robust since there is no gain margin within the range that will cause the system to move out of stability. The phase margin was set to be $60°$ which resulted in a cross over frequency of approximately 3060 rad/s.

Figure 4.8 shows the closed-loop step response for different system gains. It can be observed that the system remains stable in all cases, but the time to reach stability increases as the gain decreases.

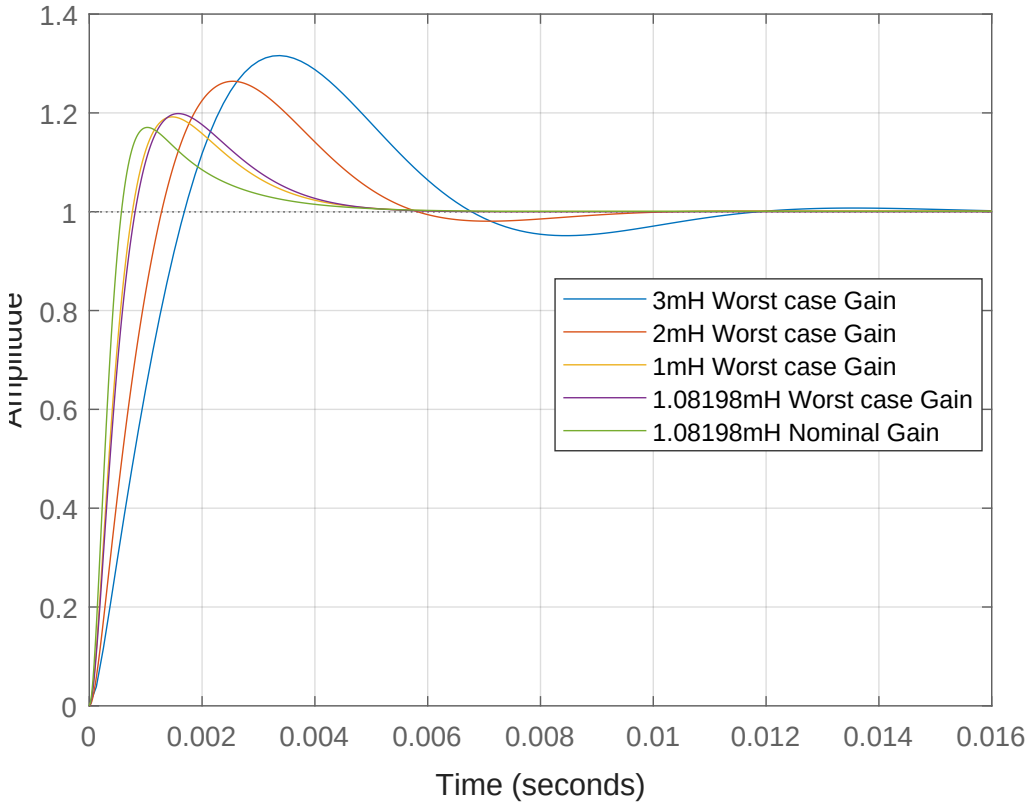

Figure 4.8: Comparison of step response with system gains

For the DC offset controller the P and I values were optimized to

$$K_P = 1.4990e - 05 \qquad K_I = 0.0025 \tag{4.20}$$

for the open loop transfer function of

$$\frac{270.008s + 45025.93}{0.0001061s^3 + s^2} \tag{4.21}$$

and were added in the DC offset controller to conduct a stability analysis of the system. A bode analysis was also conducted for the open loop system of the DC offset controller. Figure 4.9 shows the resulting bode plot.

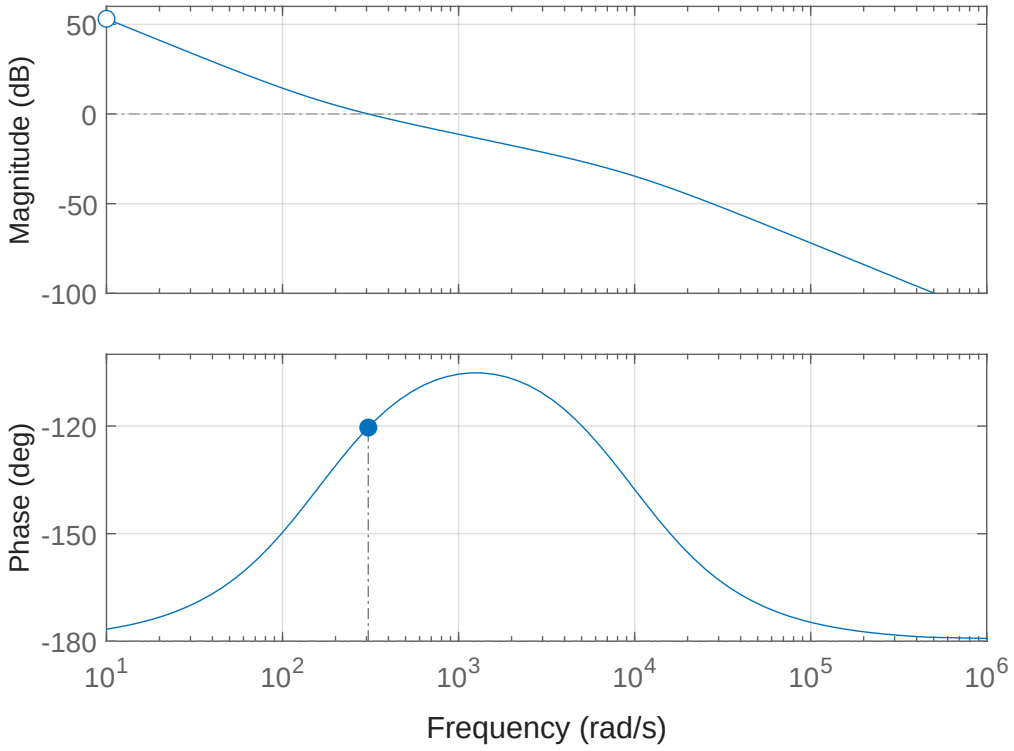

Figure 4.9: Bode plot of the open loop system for the DC offset controller

The Bode plot shows that the DC offset controller also has an infinite gain margin. One crucial characteristic of the DC offset controller is that the crossover frequency at a phase margin set to 59.6° is equal to approximately 307 rad/s. This lower cross over frequency, compared to the cross over frequency of the flux balancing controller, results in a slower system response. As designed, the crossover frequency of the DC offset controller is set to be about 10 times lower than the flux balancing controller to avoid unwanted interference between the two controllers.

4.5 Sensitivity analysis results

To understand the maximum fault that can propagate into the controllers from the current measurement, a sensitivity analysis was conducted. This analysis is mainly based on LTspice simulation results.

4.5.1 Component sweep

A simulation of the amplification circuit for an ideal case was first performed under ideal conditions, serving as a reference base simulation for comparison. In Case 1, ideal component values were used in the LTspice model. The ideal case is defined as a nominal temperature of 25 ° without taking any tolerance or component variation into account. The input voltage to the amplification circuit was defined as a triangular waveform with a peak-to-peak amplitude of 4 mV, and a frequency of 10 Hz.

This waveform represents a simulated measurement signal on the converter. From the resulting output, the gain of the amplification circuit could be calculated as

$$G = \frac{V_{p-p,output}}{V_{p-p,input}} \tag{4.22}$$

where G represents the gain of the amplification circuit, $V_{p-p,output}$ represents the peak-to-peak voltage measured at the output of the amplification circuit and $V_{p-p,input}$ represents the input voltage peak-to-peak value. The simulated output voltage for Case 1 is shown in Figure 4.10.

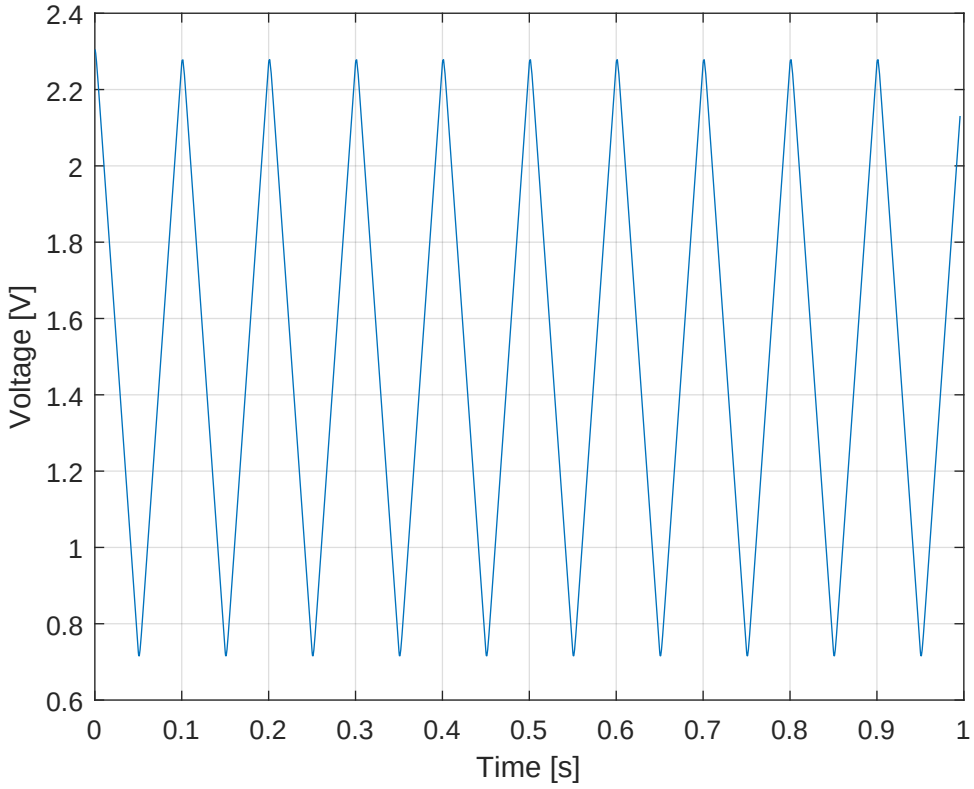

Figure 4.10: Output voltage for case 1

The peak-to-peak value of the output voltage was measured to be 1.5622 V while the average voltage was measured to be 1.4982 V. From (4.22), the gain for the ideal case could then be calculated to

$$G_{ideal} = \frac{1.5622\,\text{V}}{0.004\,\text{V}} = 390.55 \tag{4.23}$$

This gain value serves as a reference for the following simulations.

From the sensitivity analysis, it was found that the two resistors in the input RC-filter cause the largest deviations in the output voltage, resulting in a max average output voltage of 1.555 V for a $\pm 10\%$ variation. This shows that the largest deviation from the ideal case is 0.0568 V. Furthermore the four resistors in the differential OP-amp circuit caused the second highest voltage deviation of 0.0059 V when varied

with ±10%.

Overall, the analysis indicates that the two resistors in the input RC-filter, followed by the four resistors in the differential amplifier stage has the largest effect on the output voltage of the amplification circuits. An interesting observation during the analysis was that some components in the circuit could be varied by this amount without affecting the output voltage of the converter noticeably. This finding is useful, as it suggests that cost savings can be achieved by using less precise and cheaper components. Potentially even replacing the components with different ones that have other nominal values or cheaper ones that have a larger component value variation which could further save cost.

After identifying the components that primarily influence the amplification, a worst-case scenario analysis was conducted by giving the six main components their maximum or minimum values within the their tolerance range. This approach aimed to determine the maximum possible amplification error. Using the actual component tolerances, the analysis yielded a maximum average output voltage of 1.5099 V, representing a deviation of 0.0117 V from the ideal output. However, this method does not fully reflect realistic conditions, as in practice, component values vary randomly within their tolerance ranges, and some variations may partially cancel each other out. To account for this, a Monte Carlo analysis was also performed.

4.5.2 Monte Carlo analysis

To evaluate the combined impact of component tolerances and temperature variations on the performance of the amplification circuit, simulations were conducted in LTspice. These simulations focused on analyzing changes in output voltage and gain, with the goal of identifying how measurement error and gain may deviate under realistic conditions. Additionally, a worst-case condition was examined to determine the highest possible measurement error that could occur within a realistic range of operating parameters.

Two temperature cases were simulated together with the previously defined ideal case:

Case 1: $25°C$ - ideal case
Case 2: $25°C$ - nominal temperature
Case 3: $100°C$ - approximated max operating temperature of converter

Case 2 was simulated at a nominal temperature of 25 °C, with component tolerances taken into account using LTspice's Monte Carlo simulation feature. Each component's value was varied randomly within its specified tolerance range across 500 simulation runs. For each run, the gain of the amplification circuit was calculated in the same manner as in Case 1. The distribution of the resulting gain values is illustrated in the histogram shown in Figure 4.11.

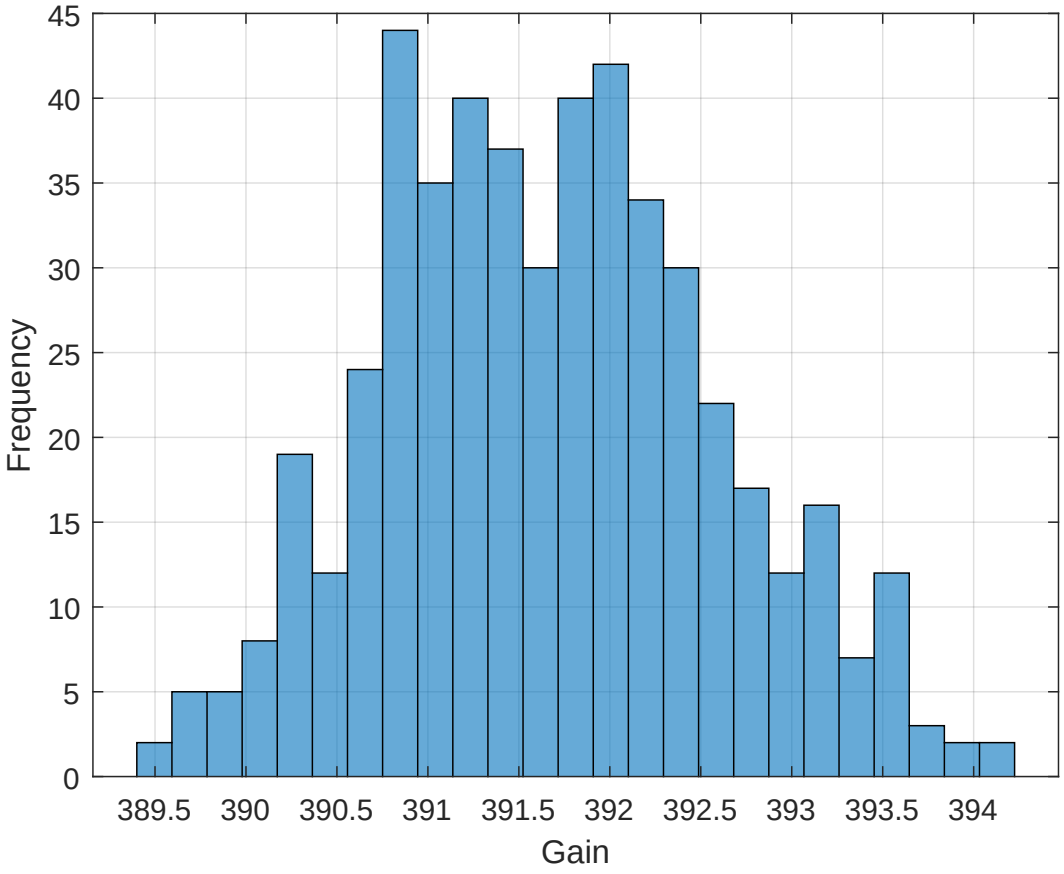

Figure 4.11: Histogram of gains for case 2

The results are centered around a mean gain of 391.6680 and appear to follow a Gaussian distribution. This suggests that the gain varies within a limited range when component tolerances are introduced. The spread of the distribution provides a visual indication of the extent of gain variation across all simulated cases.

A summary of the key statistical parameters from the Monte Carlo simulation is presented in Table 4.1.

Table 4.1: Gain statistics from Monte Carlo simulation at 25 °C

Parameter	**Value**
Mean gain	391.6680
Standard deviation of gain	0.9196
Minimum gain	389.4633
Maximum gain	394.2231
Gain range	4.7598
Maximum average voltage [V]	1.5175
Max deviation from ideal avg [V]	0.0559

The mean gain obtained from the Monte Carlo simulations at 25 °C was 391.6680, which closely aligns with the ideal gain value of 390.55. The standard deviation is

0.9196, with gain values ranging from 389.4633 to 394.2231, resulting in a total gain range of 4.7598. This indicates that, within the simulated component tolerances, gain variations remain relatively small. The average output voltage across simulations varied between 1.4423 V and 1.5175 V, with a maximum deviation of 0.0559 V from the ideal average value of 1.4982 V.

These results indicate that, under nominal temperature conditions and within the specified component tolerance ranges, the amplification circuit demonstrates stable and predictable behavior. Although minor variations in gain and average output voltage are present, the overall spread remains tightly bounded. No significant outliers or abrupt shifts were observed across the simulation data. The output remains within a predictable range, supporting its use in applications where measurement consistency is important.

To evaluate the effect of elevated temperature on the performance of the amplification circuit, a Monte Carlo simulation was conducted at 100 °C, representing the converter's estimated maximum operating temperature. As in case 2, 500 simulation runs were carried out with component values varied within their specified tolerances. Figure 4.12 shows a histogram of the simulated results.

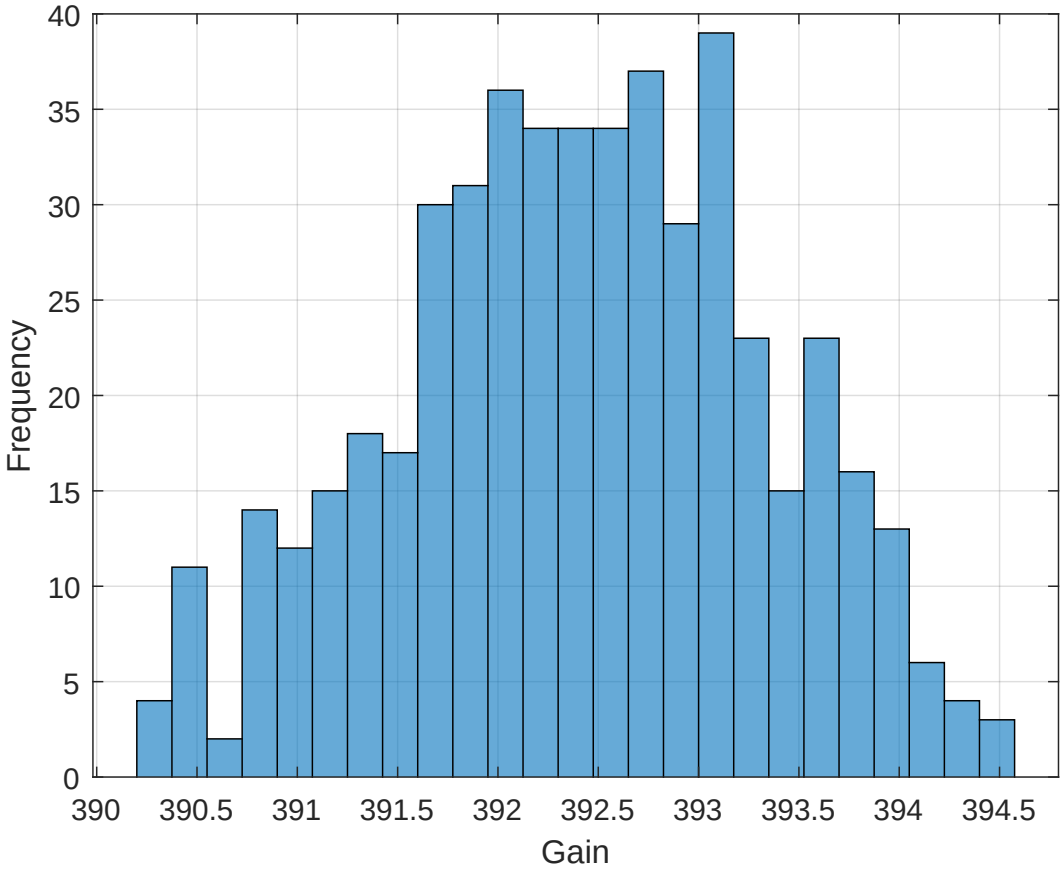

Figure 4.12: Histogram of gains for case 3

The results are centered around a mean gain of 392.4125 and show a close to symmet-

rical, normal distribution. This suggests that the gain remains statistically stable, with most simulations producing results within a relatively narrow range around the mean. The width of the distribution provides a visual indication of the gain variation due to component tolerances at elevated temperature.

The data presented in Table 4.2 provides a numerical summary of the gain variation and output behavior at 100 °C.

Table 4.2: Gain statistics from Monte Carlo simulation at 100 °C

Parameter	**Value**
Mean gain	392.4125
Standard deviation of gain	0.9206
Minimum gain	390.2154
Maximum gain	394.5541
Gain range	4.3387
Maximum average voltage [V]	1.5780
Max deviation from ideal avg [V]	0.0798

The gain values ranged from 390.2154 to 394.5541 with a standard deviation of 0.9206, resulting in a total range of 4.3387. The mean gain of 392.4125 deviates slightly from the ideal value of 390.5553. The maximum average voltage observed across the simulation runs was 1.5780 V, and the deviation from the ideal average voltage reached up to 0.0798 V. These results indicate a moderate shift in the output voltage baseline with temperature, while the gain itself remains within a limited range.

A comparison between the simulation results at 25 °C and 100 °C provides insight into how temperature influences the performance of the amplification circuit. The mean gain at 25 °C was 391.6680, while at 100 °C it increased slightly to 392.4125. Although this difference is small, it indicates a measurable temperature dependency of the gain, likely due to temperature-induced changes in component behavior.

The standard deviation of the gain was similar in both cases: 0.9196 at 25 °C and 0.9206 at 100 °C, suggesting that temperature has a minimal effect on the spread of gain values resulting from component tolerances. The gain range also remained narrow in both cases, with ranges between 4.7598 at 25 °C and 4.3387 at 100 °C.

More noticeable differences were observed in the average output voltage. At 25 °C, the maximum deviation from the ideal average voltage was 0.0559 V, whereas at 100 °C it increased to 0.0798 V. These shifts indicate that the average output voltage level is sensitive to temperature.

To isolate the influence of temperature alone, excluding the effects of component tolerances, an additional simulation was performed using ideal component values at 100 °C. The component values at this temperature were found in the manufacturers data sheets. The resulting output waveform yielded a peak-to-peak voltage of

1.5704 V and an average output voltage of 1.5027 V. From this, the temperatures effect on gain was calculated as:

$$G = \frac{1.5704\,\text{V}}{0.004\,\text{V}} = 392.6 \tag{4.24}$$

Compared to the ideal case, the gain increased by 2.05 and the average voltage increased by 0.0045 V. When compared with the Monte Carlo simulation at 100 °C, which included both temperature and tolerance effects, the ideal simulation results are close to the observed mean gain and within the expected voltage range.

4.5.3 Measurement error estimation

To summarize the fault factors, the elements affecting the measurements include tolerance-induced gain deviation, tolerance-related DC offset, temperature-induced gain deviation, and temperature-related DC offset. To define the worst-case measurement error, the maximum gain deviation from the ideal case must first be evaluated. Based on simulation results, the largest deviation occurs when combining the effects of component tolerances and temperature. The maximum gain variation caused by component tolerances is 1.1127, as seen in case 2. The additional gain shift due to temperature is 2.0468, as observed in the ideal simulation at 100 °C.

Component tolerances can vary equally in both directions one amplification circuit might experience a positive deviation while the other experiences a negative one. In contrast, temperature induced variation is generally unidirectional, since it's unlikely that one part of the circuit would be below zero while another reaches the maximum operating temperature. Therefore, the worst-case gain deviation is defined as twice the component tolerance deviation plus the temperature-induced gain variation, resulting in a total worst-case gain deviation of 4.2722. Therefore, the worst-case gain deviation ΔG is defined as 4.2722, as it represents the largest possible deviation.

However, ΔG caused by both temperature and component tolerances are not critical, as they only impact the converter when a DC offset is present in the primary side current. In the absence of a DC offset, the controller can drive the magnetizing current to zero regardless of gain mismatches, since there is no persistent error to prevent it from settling. This relationship between the gains and offsets can be explained by

$$\begin{aligned} V_{sense} &= R_{Shunt}(G_1 i_p + G_2 i_s)) \\ &= R_{Shunt}((G_1 - G_2) i_p + G_2 i_m) \end{aligned} \tag{4.25}$$

where V_{sense} is the difference in sensed voltage between the two amplification circuits and G_1, G_2 are the gains of the first and second amplification circuits, respectively. R_{Shunt} is the shunt resistor used for the current measurement. The shunt resistors

are assumed to have negligible tolerance variation, as both measurements are taken on the same PCB and will therefore most likely have equal resistance. If separate PCBs were used, the tolerance differences between the shunt resistors would need to be considered.

Using the assumption that the controllers always regulate the DC offset of i_p to zero together with the assumption that i_m is controlled to zero. The gains of the amplification circuits no longer affect the current. However, if a DC offset were to occur in the primary current, the gains would have an effect. For example, a DC offset of 1 A would result in an amplified offset of 0.854 44 mV for the worst case tolerance and temperature gain scenarios. This highlights the importance of the DC offset controller, as by minimizing the DC offset in the current the accuracy of the measurement can be improved which improves the functionality of the flux-balancing controller.

In the model used in this thesis, two identical amplification circuits are used for current measurement, one for the primary current and one for the secondary current. Figure 4.13 illustrates a simplified version of how these signals are amplified and calibrated to estimate the magnetizing current.

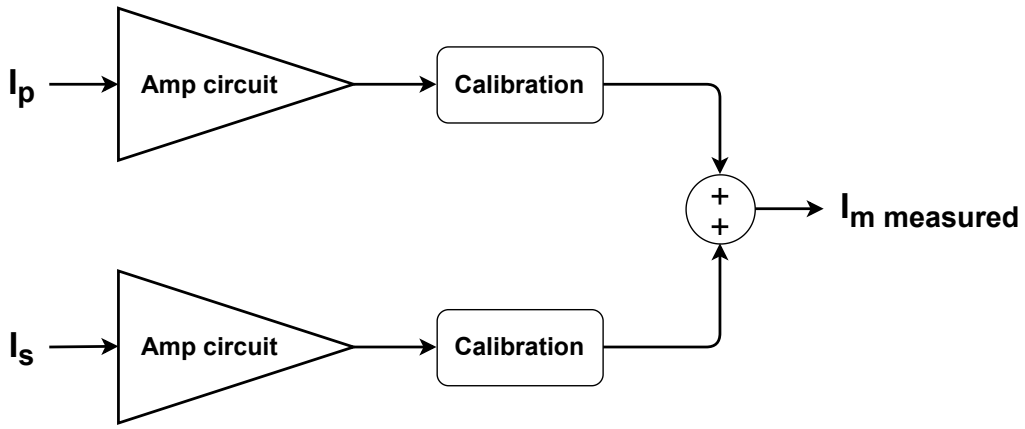

Figure 4.13: simplified model of amplification and calibration signal during startup

Both the primary and secondary current signals are calibrated at startup of the converter. This means that during system initialization, the output of the amplification circuit is calibrated to zero based on a known input value. This process removes the offset variations caused by component tolerances. However, it does not eliminate all offset variations due to temperature, as it only corrects for the conditions present at startup. As the converter operates, its temperature is likely to rise, and any resulting offset changes are not accounted for by the initial calibration.

Because of this temperature variations can still introduce an offset in the amplification circuits. In the worst-case scenario, the temperature difference ΔT between the circuits reaches 75 °C. To quantify the temperature induced offset error, the ideal average output voltage ΔV is computed. In the simulation, the ideal average output

voltage at 100 °C was 1.5027 V, representing a deviation of 0.0045 V from the 25 °C ideal case. This output voltage deviation can be translated to the current deviation Δi using

$$\Delta i = \Delta V_0 \cdot \frac{1}{G_{nominal} R_{Shunt}} \tag{4.26}$$

where G_{nominal} is the ideal gain and R_{Shunt} the shunt resistance which is estimated to be 200 $\mu\Omega$. The current deviation for this simulation was then calculated using

$$\Delta i = 0.0045\,\text{V} \cdot \frac{1}{390.5553 \cdot 200\mu\Omega} = 57.61\,\text{mA} \tag{4.27}$$

If assuming that the error increases linearly, and the temperature ranges between 25 °C - 100 °C, the voltage error per degree C on the input of the amplification circuit is calculated to 0.153 627 μV/°C. The current estimation error per degree Celsius is approximately 0.768 133 mA/°C. This potential error must be considered when analyzing the system's response in Simulink, particularly in evaluating the peak step response.

4.6 Dead-time effect on magnetic flux

During simulations, an unexpected spike in the magnetizing current consistently appeared at the start of each run. This initial peak also appeared when comparing simulation results to hardware measurements. In the hardware, the spike naturally settled to 0 A due to self-regulating behavior, while in the Simulink model, the controllers were required to bring the current down to 0 A. Further investigation revealed that this initial spike was caused by a large inrush of magnetic flux into the transformer. This can be explained by the shape of the voltage that is applied to the the transformer. As shown in Figure 4.14.

It can be observed that, due to the voltage waveform being either positive or negative, the current responds with an immediate rise or fall upon the application of voltage. Subsequently, the current decreases by the same magnitude as the initial change when the opposite polarity is applied. This behavior leads to the current attaining a net positive or negative average value following the initial application of voltage instead of centering around zero. To reach an average zero current over time, this imbalance must be controlled.

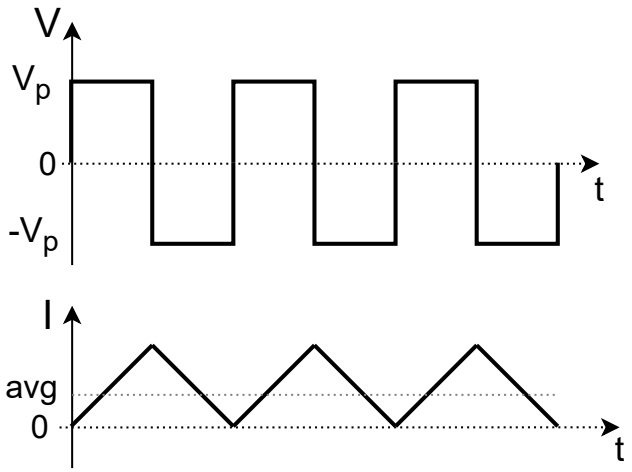

Figure 4.14: Diagram showing how the initial spike in current is created

However the self regulating behavior observed in the hardware was a result of a dead-time effect present in the system. To investigate this, a model was constructed in LTspice to determine the effect of dead-time on the magnetic flux inside the core. The model consists of a base model of a full bridge converter with ideal switches and a 1 mH inductor as the load. The value was chosen to resample the one in the real converter. The inductor was initiated with a current of 5 A at the start of the simulation. The model can be seen in Figure 4.15.

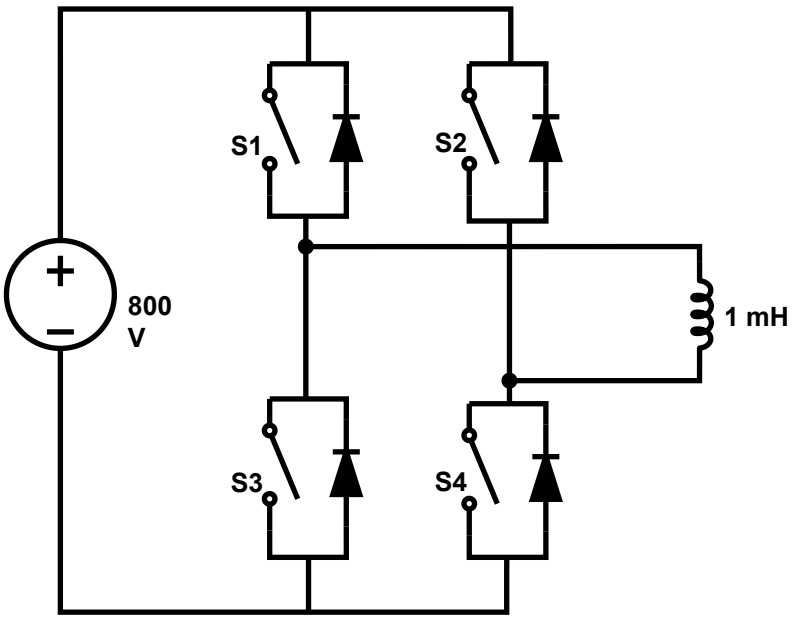


```
S1: PULSE(0 5 0 10e-9 10e-9 {Don} 2e-6)
S2: PULSE(0 5 1e-6 10e-9 10e-9 {Don} 2e-6)
S3: PULSE(0 5 1e-6 10e-9 10e-9 {Don} 2e-6)
S4: PULSE(0 5 0 10e-9 10e-9 {Don} 2e-6)

.ic I(L1)=5
.model SW SW(Ron=0.1 Roff=1Meg Vt=0.5 Vh=-0.4)
.step param Don 0.85u 0.95u 0.025u
.tran 0 0.25m 0
```

Figure 4.15: LTspice model for dead-time effect on flux investigation

To generate the switching pattern for the ideal switches, voltage sources using the **PULSE** function were employed. These sources output a high signal (5 V) to activate the switches and a low signal (0 V) to deactivate them. The rise and fall times were set to 10 ns, and the total duration of one switching period was defined as 2 μs. The system's dead-time was controlled by adjusting the variable D_{on}. In this simulation, D_{on} was swept from 0.85 μs to 0.95 μs in increments of 0.025 μs. The dead-time for one switching period was calculated as

$$T_{Dead-time} = T - 4T_{Rise/fall\ time} - 2D_{on} \tag{4.28}$$

where $T_{\text{Dead-time}}$ is the total dead-time per switching cycle, T is the switching period

(20 μs), and $T_{\text{Rise/fall time}}$ is the specified rise/fall time (10 ns). Based on this relationship, it can be observed that the dead-time decreases as D_{on} increases. For the swept range of D_{on}, the calculated dead-time varied between 60 ns and 260 ns.

The total time for the simulation was set to 0.25 ms. The results of the simulation can be seen in Figure 4.16.

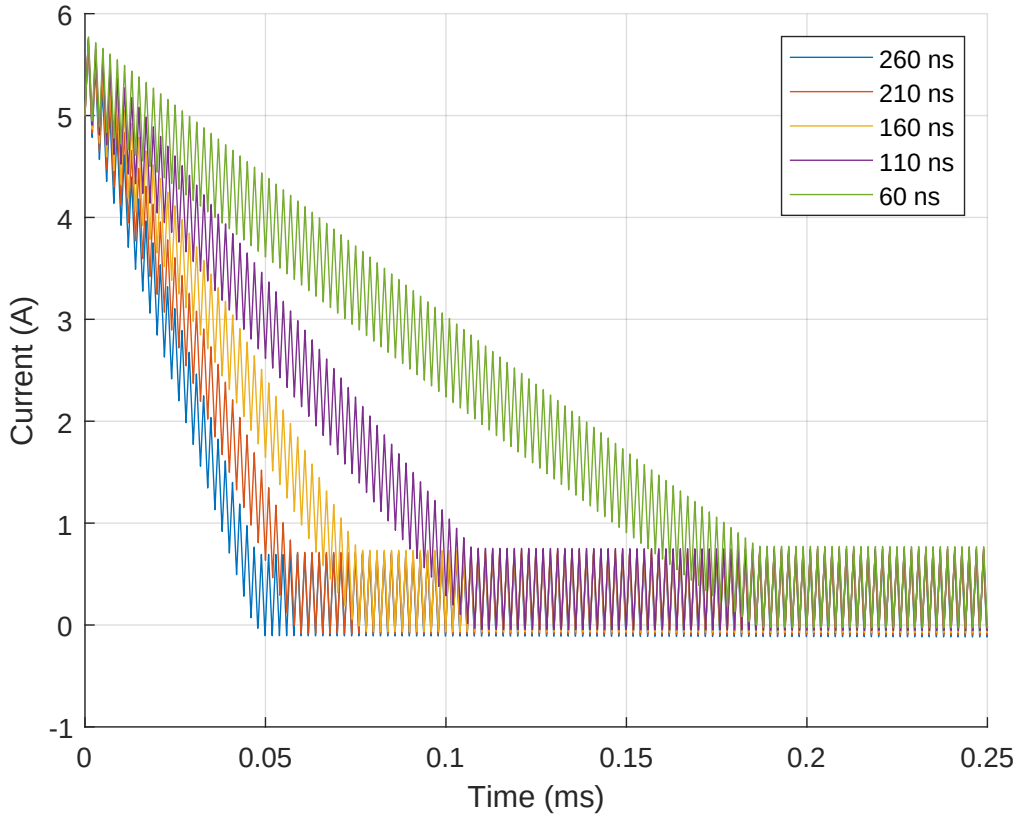

Figure 4.16: Dead-time impact on magnetizing current results (positive current)

The behavior of the current flowing through the inductor reflects the characteristics of the magnetizing current. Simulation results show that this current self-regulates to a value close very close 0 A, and that a longer dead-time causes it to reach 0 A more quickly. When the current through an inductive load suddenly increases a DC offset component appears, but this offset only decays when dead-time is present. These results demonstrate that dead-time can be used to passively reduce the magnetizing current.

The previous simulation was performed again but with an initial current of -5 A instead to verify the behavior. Figure 4.17 shows the simulation results.

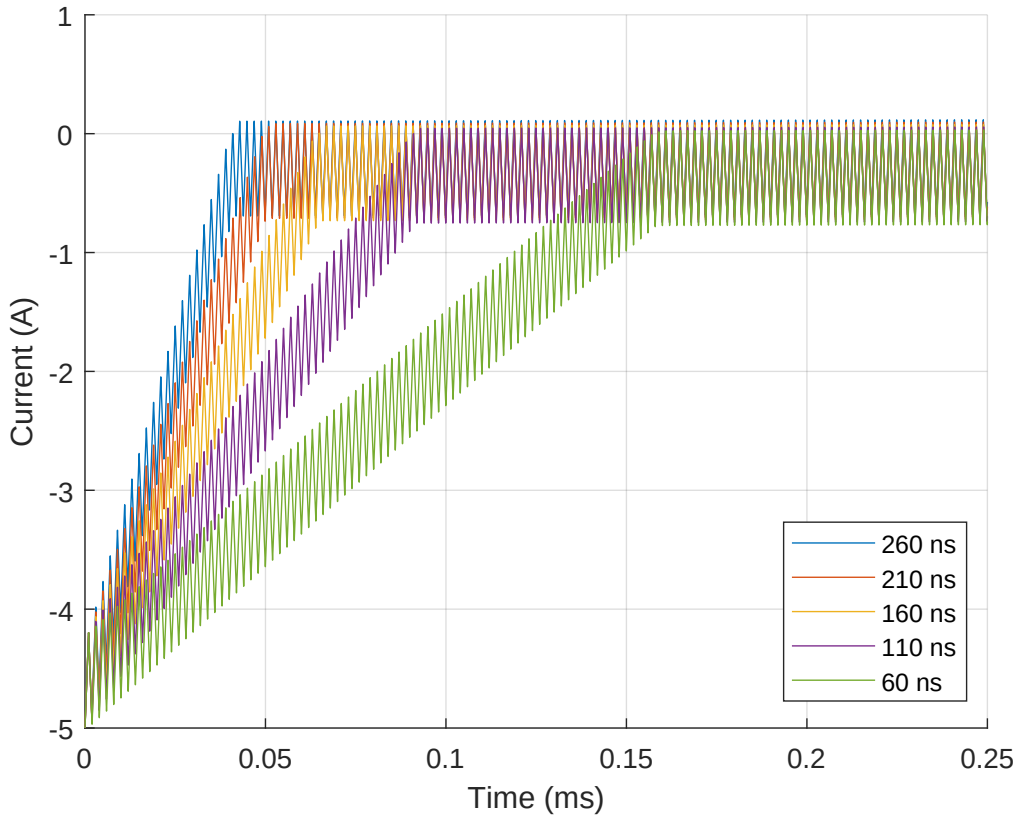

Figure 4.17: Dead-time impact on magnetizing current results (negative current)

The results demonstrate behavior consistent with the previous simulation. The current approaches 0 A, and does so more rapidly as the dead-time increases, but with reversed polarity. This explains our previous observation and was investigated further.

The self-regulating behavior can be explained by analyzing the voltage across the inductor. Figure 4.18 shows how this voltage varies in relation to the switching patterns of Switches 1 and 2 (scaled by a factor of 100 for clarity), along with the inductor current. In this case, the inductor is initialized with a current of -5 A.

It can be observed that when the inductor current is negative, the voltage across the inductor remains positive for a longer duration than it is negative. Comparing this to the switching signals, it becomes clear that this positive voltage occurs during the dead-time. In contrast, when the inductor is initialized with a current of 5 A, as shown in Figure 4.19, the opposite behavior is observed. Here the voltage becomes negative during the dead-times to compensate for the current's opposite polarity.

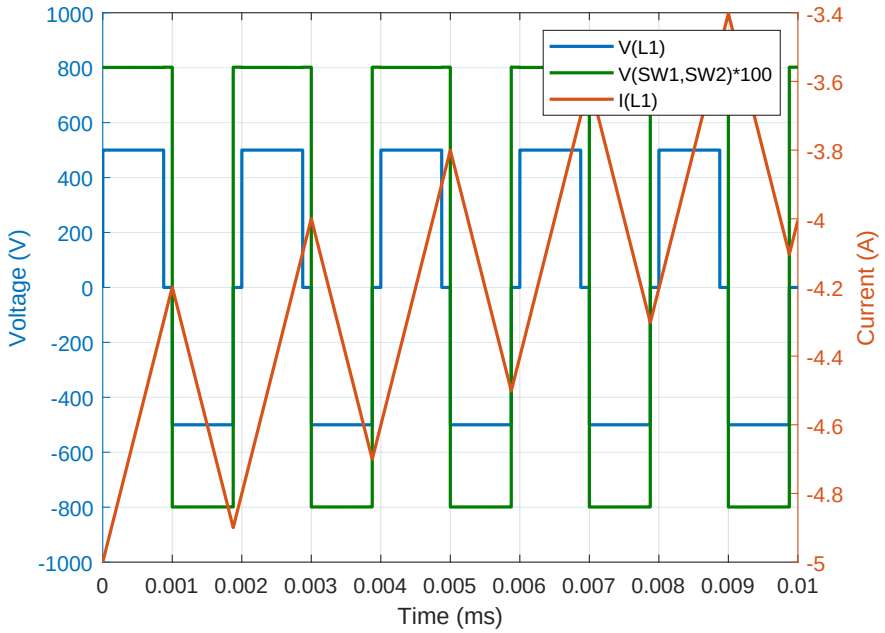

Figure 4.18: Current and average voltage over inductor (negative)

This demonstrates that the voltage opposes the direction of the current, helping to drive it back toward zero. The effect becomes more pronounced with increased dead-time, as the extended interval allows the voltage to maintain a higher average value opposing the current. This results in a faster reduction of the current toward zero. This is the dead-time effect.

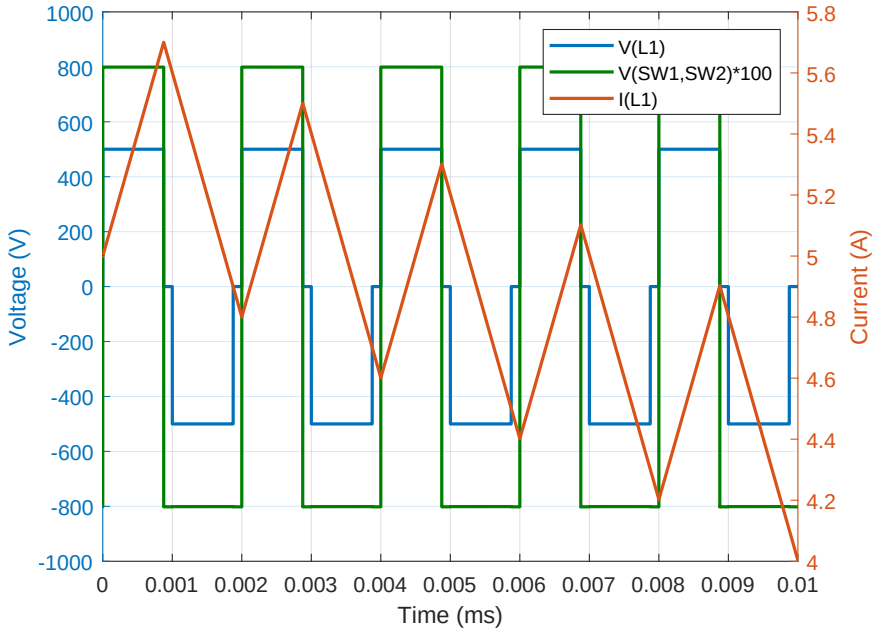

Figure 4.19: Current and voltage over inductor (positive)

Figure 4.20 shows the same plot after the current reaches a value close to zero. Here it is observed that the voltage is on for half of the dead-time and off for half, resulting in an average value of zero no longer opposing the current.

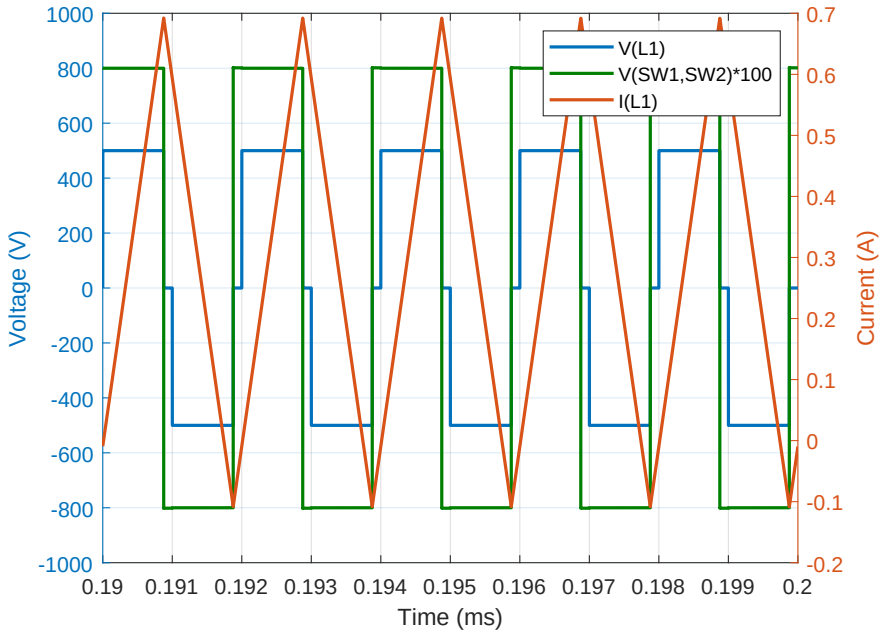

Figure 4.20: Current and voltage over inductor after reaching zero

4.6.1 Simulink implementation of dead-time effect

To emulate the dead-time effect observed in the hardware, a simple Simulink block was added. The model can be seen in Figure 4.21.

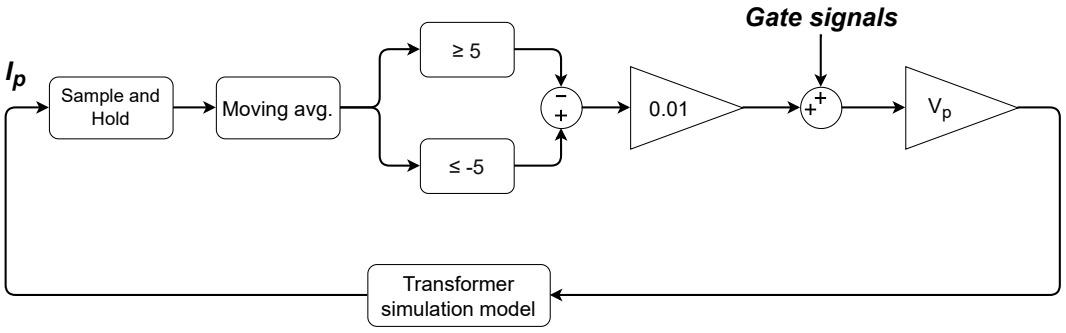

Figure 4.21: Model of dead-time effect implementation in Simulink

The Simulink block works by taking the primary side current as input. The signal is then put through the moving average filter and compared against a threshold values of ± 5 to tell if the magnetization current has drifted above or below the zero level. 5 A was used since it is a value larger then the ripple in the magnetization current which means that by reaching that value you are already getting the full correction

offset effect from the dead-time. These values work in simulation and were chosen for that reason. However, they are not scientifically derived and could likely be lower, though they approximately replicate what was observed in practice. Instead this serves as an implementation to fix the simulations. This simple model therefore does not consider the dead-time effect until it reaches its maximum capacity. The effects of dead-time before this point proved more complicated to model and are assumed to be small enough that this implementation is enough to achieve sufficient simulation accuracy.

If the magnitude of the current is larger or equal to 5 a value of 0.01 is added or removed from the primary side voltage depending on the sign of the current. This gain factor is proportional to the system's dead-time characteristics. Since the primary current and voltage are directly linked, this method offers a fast and effective way to counter act offsets. It creates an input in the opposite direction when an offset is present. While this implementation does not accurately model the dead-time effect, it serves as a functional workaround for simulations. It successfully introduces offset correction, which is the effective role of the dead-time in this case, thereby making the simulations more closely resemble behavior in practice. This implementation also slightly interferes with the DC offset controller, as it limits the current so rapidly that it reduces the control signal, preventing further integration. However, the effect is minimal and has therefore been considered negligible.

4.7 Hardware implementation

The hardware implementation of the control system consists of several different steps including current measurement, amplification circuitry, controller implementation together with feedback implementation. A schematic showcasing how this is implemented can be seen in Figure 4.22. The current sensing and the amplification circuits required was provided by Aros Electronics AB.

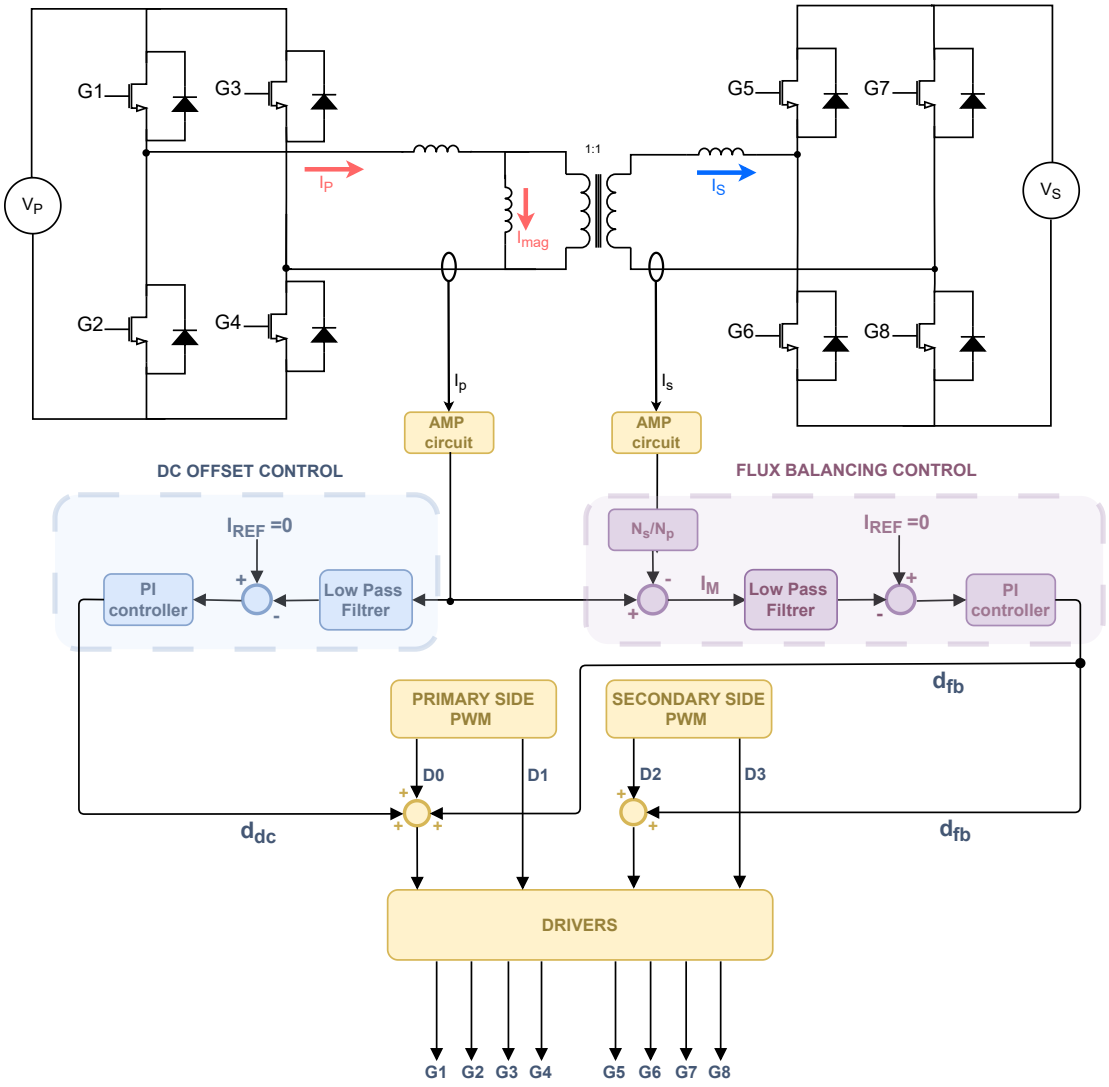

Figure 4.22: Hardware implementation overview

4.7.1 Shunt current sense

To sense the current in the hardware, shunt current sensing was used. However, instead of a dedicated resistor, the existing copper trace in the circuit was utilized. As discussed earlier, this results in a very small voltage drop to measure. Because of this the use of amplification circuits was needed.

4.7.2 Amplification circuits

To develop an accurate Simulink model, a comprehensive analysis of these circuits was conducted to understand their signal filtering characteristics. The analysis identified three primary components contributing to signal filtering:

1. **Initial Low-Pass Filter**: This stage exhibits low-pass characteristics with a bandwidth of approximately 4080.892 Hz.

2. **Secondary Low-Pass Filter**: Functioning as an additional filtering stage with low-pass characteristics, this component has a bandwidth of 1590.154 Hz.

3. **Operational Amplifier Bandwidth Limitation**: The op-amp's inherent bandwidth limitation, determined to be 11 482 Hz by dividing the Gain bandwidth product (GBW) from the datasheet by the closed loop gain in our use case.

The three filter components were combined by summing their respective transfer functions in MATLAB. The resulting equivalent transfer function showed a 3 dB cutoff, corresponding in a drop of $\frac{1}{\sqrt{2}}$ at the peak value at 1554.40 Hz. This frequency was used in the Simulink model to apply filtering to the current signal before it was fed into the controllers. This approach was chosen to replicate the behavior of the physical hardware, where the signal is filtered during amplification prior to the control input. Several alternative low-pass filter designs were explored to evaluate whether a steeper cutoff would offer improved performance. However, a first-order low-pass filter was ultimately selected for implementation.

4.7.3 Flux balancing controller implementation

The flux balancing controller is implemented to control the average magnetizing current I'_m to zero while the PI controller outputs a duty cycle. This small change in duty cycle is then inserted on both the primary side PWM leg as well as on the secondary side PWM leg. This controls I'_m to zero by applying a small change to the duty cycle on the primary side and a small change in the opposite direction on the secondary. The difference in duty cycle creates a difference in voltage which causes the current to correct itself. This small change is enough to not effect the power transfer noticeably while still controlling the magnetizing current.

4.7.4 DC offset controller implementation

The DC offset controller is implemented in a very similar way to the flux balancing, however instead of controlling the magnetizing current it controls the average primary side current I'_p to 0. This is only inserted on the primary side PWM leg. When the DC offset controller pushes I'_p current to 0 A our flux balancing controller will control the secondary current to 0 A as well. Since the magnetizing flux is the difference between the primary and secondary side currents according to our state-space model. This way this controller prevents our primary and secondary side currents from drifting apart.

4.8 Analysis of simulated control

In this section, the results and analysis of the simulations are presented. All current waveforms shown are taken from after the low-pass filters to improve clarity. In practice, these are also the currents that are fed to the converters. For the primary and secondary currents, the secondary current is inverted before plotting to better illustrate their relationship. In practice, the primary and secondary currents have opposite signs due to traveling in different directions from each other.

All simulations were performed using Simulink with a maximum step size of $1ns$ and a relative tolerance of $0.1\mu s$. This level of accuracy was necessary, as even slightly relaxed settings had a significant impact on the results. However, it also resulted in very long simulation times. Despite the extremely fine step size, some simulations still exhibit a very small steady-state error due to sampling. This error was considered minimal enough that it was acceptable for the purposes of the analysis.

The transformer used in this thesis is calculated to saturate at a value of 2.8 A. However, this is a theoretically calculated value assumed for symmetrical flux. For the planar transformer with a square shape, different parts of the transformer would saturate more quickly. Due to the desire to avoid pushing the transformer into saturation and risking damage to any components, an exact saturation value was never determined experimentally. The threshold value of 2 A was instead chosen to represent saturation in simulations, allowing for a clear assessment of the results. This also provides a small safety margin for the converter. In practice, operating even this close to the saturation region would be risky and the threshold value of 2 A will be considered to be the limit at which the converter saturates for all following simulations.

4.8.1 Case 0

The simulated average magnetizing current I'_m is shown in Figure 4.23. Initially, the current rises due to the inrush of magnetic flux into the transformer. It then reaches a steady state until a voltage step is applied at 7.5 ms. Following the step, I'_m begins to rise linearly, crossing the saturation threshold of 2 A after approximately 17 ms. This clearly demonstrates how quickly even a small imbalance in voltage can drive the transformer into saturation. The simulation does not account for dead-time, which would slightly delay the onset of saturation. However, even with dead-time included, the transformer would still saturate within a few milliseconds. This highlights the importance of fast and accurate control. In practical operation, where the converter runs continuously for extended periods, even a minor voltage difference can cause near-instant saturation within this time frame.

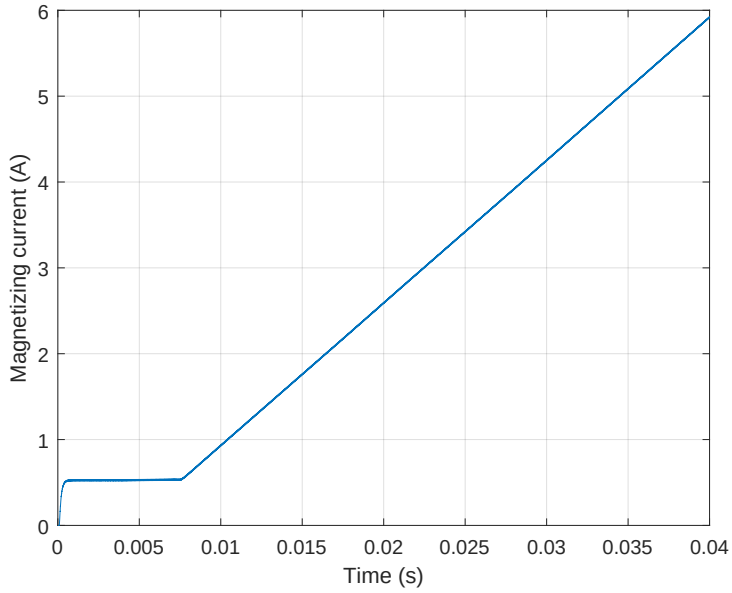

Figure 4.23: Simulated magnetizing current of standard case

Figure 4.24 shows the average primary and secondary currents, I'_p and I'_s, during simulations for case 0. It can be observed that the y-axis of the figure displays extremely large current values. This is due to the model not including any resistances, which causes the currents to increase indefinitely in the simulation if left unchecked by the controllers. In practice, these currents would be kept at much lower levels due to parasitic elements and other losses.

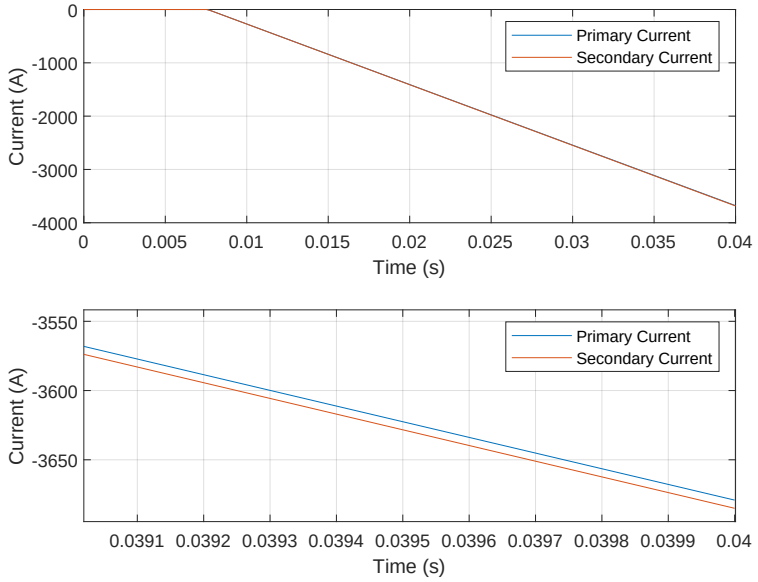

Figure 4.24: Simulated currents of standard case

As observed in the lower plot in Figure 4.24 The currents have started to separate slightly. However are generally kept at equal magnitudes

In practice, when losses and parasitic elements are taken into account, the current can still reach magnitudes that may lead to serious issues. To address this, a DC offset controller is implemented to regulate the net current to zero. This ensures that both currents remain within the measurement range of the hardware and prevents them from rising to levels that would increase losses or damage components. Additionally, it helps prevent the accumulation of a DC offset in either current.

4.8.2 Case 1

The simulated I'_m in case 1 is shown in Figure 4.25. Although the signal shows a clear peak whenever a step is applied as well as at the start of the simulation. It can clearly be observed that the system manages to reach a value close to zero quickly after each instance. It is also clear that the controller never comes close to instability while still accomplishing quick and efficient mitigation of the errors. Removing the 0.5 V step at 15 ms produces an equally sized step in the opposite direction, since the controllers had already compensated for the initial voltage change.

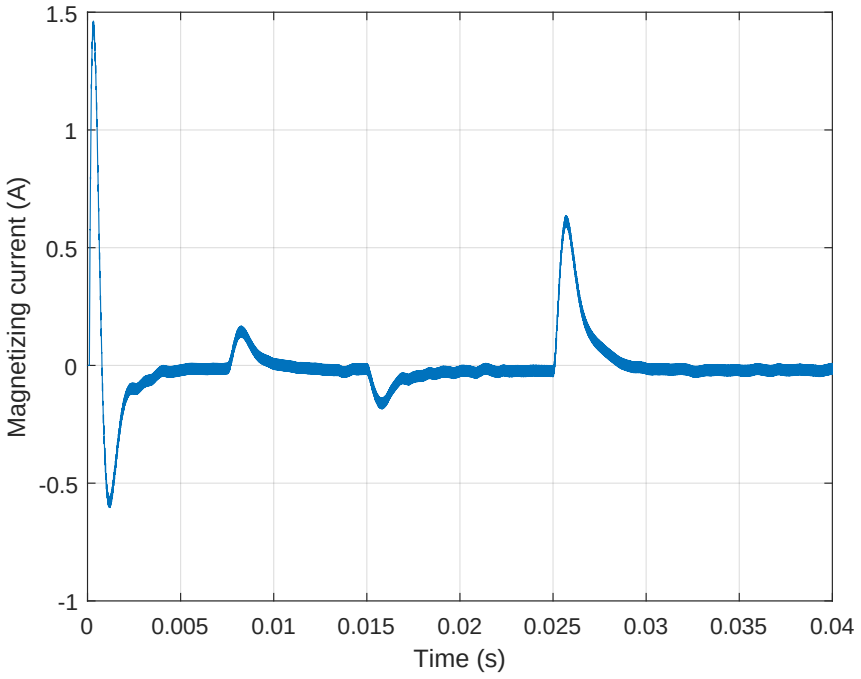

Figure 4.25: Simulated average magnetizing current for case 1

At 0.0075 s when the 0.5 V is applied a maximum current of 0.1609 A is reached. Similarly when the step is removed the current reaches a maximum of -0.1616 A. As expected a significant peak is recorded when the step of 2 V was applied reaching a maximum value of 0.6357 A. Even at this step the current stays well below the

saturation region of the transformer. In practice, a voltage step on one side of the transformer may result from the nonlinear behavior of the MOSFETs. This can cause by slight imbalances in heating, leading to a small voltage difference between the MOSFETs. However, this difference is typically much less than 2 V, and even 0.5 V is likely an overestimate. This highlights the system's robustness and its ability to prevent saturation, ensuring stable operation even under demanding conditions. As discussed earlier, the initial step observed at the start of the simulation is caused by inrush current when the transformer is first energized. In this case, the current reaches a very high value, but only for a very short duration.

Figure 4.26 shows I'_p and I'_s for case 1. As observed, the current levels remain within reasonable magnitudes. At first glance, it may appear that the controller fails to drive the currents to zero after each step. However, this behavior is intentional as the current-balancing controller is deliberately designed to be ten times slower than the flux-balancing control loop. Within such a short time frame, the DC offset controller does not have sufficient time to bring the currents to zero. In extended simulations, the controller effectively drives the currents to zero between steps. However, in the simulations presented here, this additional time is deliberately omitted to more easily display system behavior and test the systems performance under more demanding conditions. It can however be observed that the controllers still manage to keep the currents together. After each step the currents drift apart slightly but are quickly controlled together again.

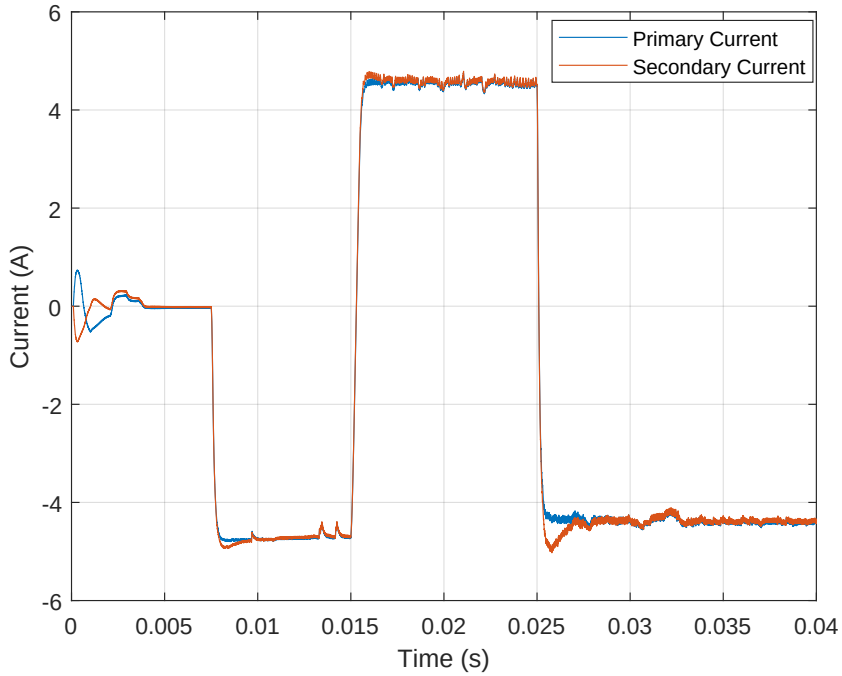

Figure 4.26: Simulated current response for case 1

Some key observations include the system's response to the initial 1 V step input, where the currents initially move in opposite directions. The dead-time effect in combination with the DC offset controller limit the current step so that both currents

reach a steady state. The DC offset controller then gradually accumulates integral action, slowly driving I'_p back toward zero. Simultaneously, the flux-balancing controller pushes I'_s to match the primary, causing both currents to converge towards zero. This process is abruptly interrupted when the step is removed at 0.015 s, triggering a similar response in the opposite direction. Since the initial position for the second step is below 0 A, the controllers have additional time to accumulate the error. This results in that the DC offset controller together with the dead-time effect manages to stabilize the currents at a lower magnitude compared to the initial step.

The third step interrupts the currents before they have time to fully stabilize or accumulate sufficient integral action to return towards zero. This sudden increase pushes the current close to the -5 A range, causing a brief mismatch between I'_p and I'_s. This is followed by a slow buildup of integral action in the DC offset controller, which gradually begins to steer the currents back towards zero.

When testing on hardware it was observed that the converter could operate without the DC offset controller implemented, contrary to the conclusions drawn from this simulation. In practice the separating behavior could only be observed to a minor degree which did not effect the converter noticeably. This was investigated and deemed to be caused by the dead-time effect inside the converter. In practice, at least for some values of dead-time, the dead-time effect seems to be sufficiently eliminating DC offsets in the primary and secondary currents. This was not studied extensively and would require further investigations, although the results look promising. The DC offset controller did however, perform better at limiting and balancing the currents in the hardware when implemented, even though operation was possible without it. If these improvements are to minor they might not be necessary and might not justify the added complexity and cost of implementing the additional controller in practice.

4.8.3 Comparison with hardware

Figure 4.27 shows the response of both the simulated model and the hardware system when a reference step of 0.2 A is applied. In this case, a reference step is used instead of a voltage step, as applying a voltage step is not possible in the hardware without adding extra functionality. To enable easier comparison, the same reference step is also applied in the simulated model.

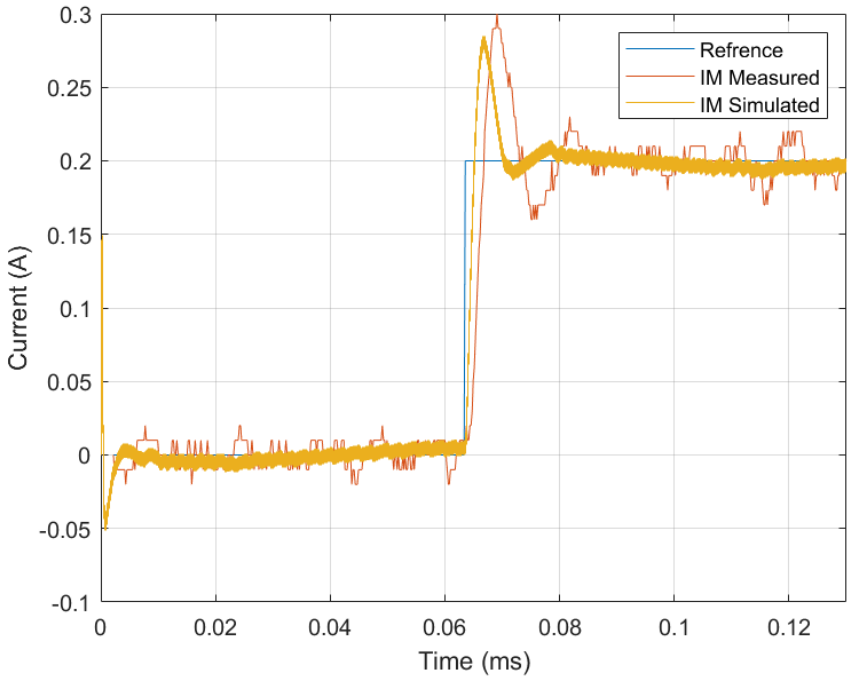

Figure 4.27: Comparison between magnetizing current response between hardware and simulation.

For this setup, the primary and secondary voltages were set to 850 V and 550 V respectively and a 20 kW load was applied. In the hardware measurements, I'_m was sampled at a frequency of 10 kHz. As observed, the simulated response exhibits a faster rise time than the experimental one with rise times of 1.5445 ms and 3.187 ms respectively. The hardware response also exhibits slightly more oscillation after the initial overshoot compared to the simulated response, but remains well within the stability margins. The difference in rise time of almost twice the size was unexpected and indicate that certain aspects of the hardware behavior might still remain unmodeled in the simulation. One feature that could contribute to this is the dead-time effect which could require better modeling to achieve more accurate results. Another factor here is the exact inductance value of the transformer. For the simulation the measured values were used but as previously discussed the inductance can vary noticeably.

Nevertheless, the results are very promising demonstrating faster control dynamics than initially expected. Both systems achieve a rapid and effective error mitigation, which is more than sufficient for the intended application. The hardware behavior is also clearly reflected in the simulation and is therefore considered an accurate enough representation of the converter to support continued analysis using simulation.

4.8.4 Case 2

For case 2, the worst case operating condition for the converter was investigated with the same setup as seen in case 1 to investigate the operating point of the converters effect on stability. The steps applied to the model are the same as for case 1 and follow the magnitudes and times specified in Table 3.2. The resulting I'_m step response can be seen in Figure 4.28.

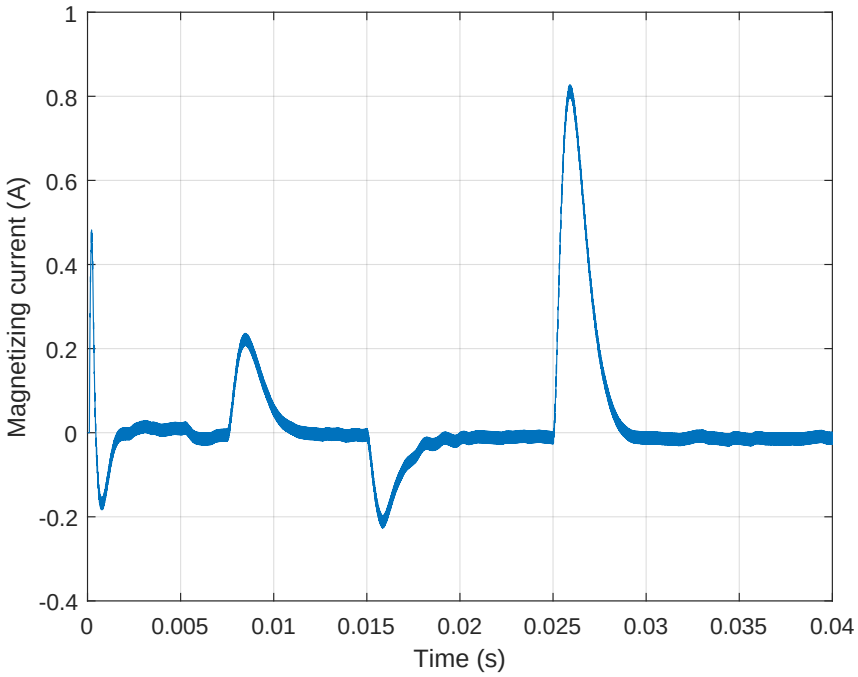

Figure 4.28: Simulated magnetizing current for case 2

As observed in the step response of I'_m, the behavior closely resembles the step response seen in case 1. The initial step of 0.5 V, applied at 0.0075 s, results in a current peak of 0.2229 A, which is higher than that observed in case 1. This outcome is expected, as the increased voltage difference across the converter introduces more challenging control conditions. Nevertheless, the system still achieves a near-zero value rapidly, although it is slightly slower than in case 1. This swift stabilization following each step demonstrates the robustness of the control system.

When the voltage step is removed at 0.015 s, a corresponding negative peak of -0.2207 A is observed, mirroring the initial response. For the third and larger voltage step of 2 V, applied at 0.025 s, the peak current reaches 0.8258 A and the response is significantly more pronounced compared to case 1. As a result, the transformer operates closer to its saturation limit. Although the controller responds nearly as fast as for case 1, the substantial increase in current emphasizes the importance of operating conditions to prevent saturation of the transformer. Consequently, the following case will examine the worst-case operating point to ensure a sufficient margin of error, even under the most demanding operating conditions.

Another interesting observation is the initial current peak caused by the inrush of magnetic flux into the transformer. Interestingly, this peak is lower in the second case simulation compared to the first, despite expectations to the contrary. Case 2 also showcases slightly less stability in the initial stages when the current is controlled to zero before the initial step is applied. The step responses of I'_p and I'_s for case 2 are shown in Figure 4.29.

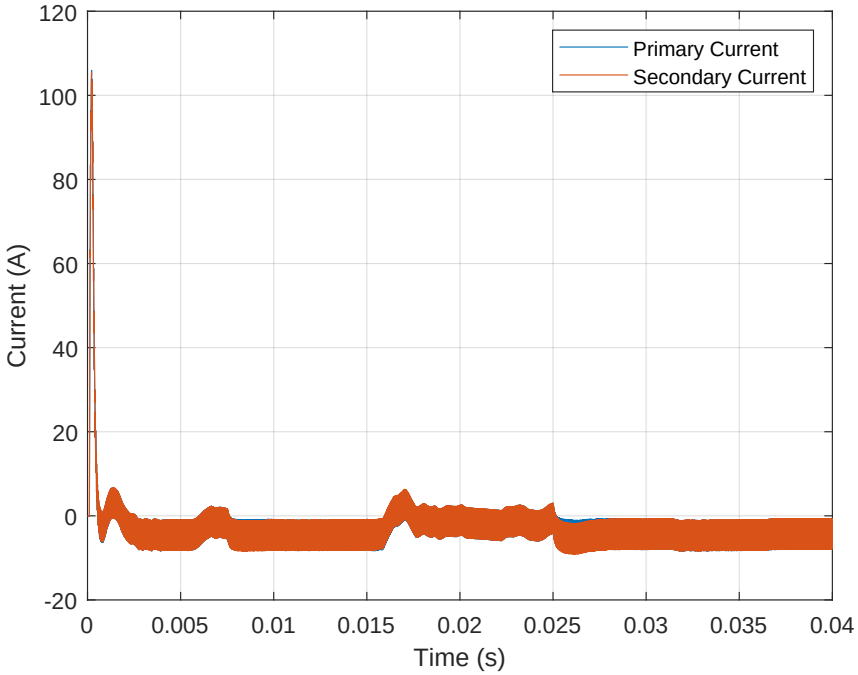

Figure 4.29: Simulated currents for case 2

An important observation here is that I'_p and I'_s exhibit a significantly higher initial peak compared to case 1. This may be attributed to how the initial currents are computed within the state-space model, particularly when a large voltage difference exists between the primary and secondary sides coupled with the phase shift between the primary and secondary voltages. In this case, the phase shift limits the initial current peak in the transformer, but results in larger current values in both the primary and secondary windings compared to Case 1.

Similar behavior to Case 1 is observed for the currents, but with significantly more ripple throughout the simulation. The increased ripple is primarily due to the phase shift, which introduces more fluctuation as the currents deviate from the 0° phase used in Case 1. Additionally, the higher overall voltage and the larger voltage difference between the primary and secondary sides contribute to a larger initial peak. The current does not stabilize at zero before the next step is applied. Instead, it settles at a value close to 5 A. This is likely the cause of the reduced stability observed at the beginning of I'_m. Although this behavior is not optimal, it would typically be addressed by the DC offset controller, as discussed earlier. However, due to the short simulation time, the system is required to respond to the steps before it can reach a steady state. This setup was intentionally chosen to simplify comparison

and test the system under more challenging control conditions. It is important to note that, despite this behavior, the system effectively keeps I'_m near zero, successfully preventing core saturation, which is the primary function of the controllers.

It is also important to note that the difference in I'_m between Case 1 and Case 2 was more pronounced with different PI controller values. However, after tuning the controllers, the optimized gains resulted in significantly better control, reducing the difference between the cases noticeably.

4.8.5 Case 3

In case 3, the largest voltage step that could be applied to the worst-case scenario was investigated. After simulation, it could be established that the largest voltage step that could be applied in the Simulink model without reaching saturation was 4.9 V. Figure 4.30 shows I'_m when first applying and removing a 0.5 V followed by the 4.9 V step.

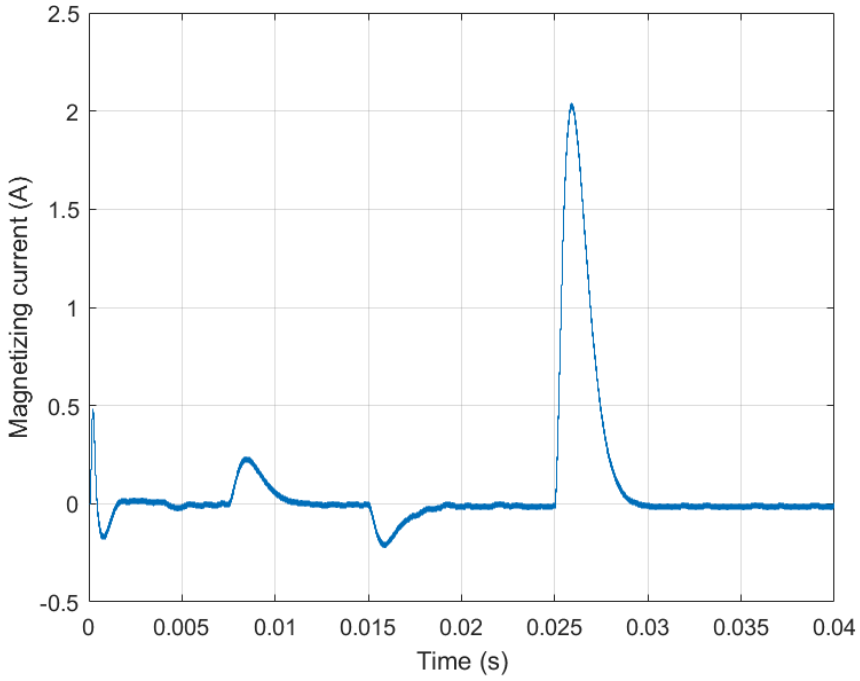

Figure 4.30: Simulated magnetizing current response for case 3

As shown in Figure 4.30, I'_m reaches approximately 2 A shortly after the step input is applied at 0.025 s. In a practical scenario, the transformer is unlikely to enter saturation despite the current reaching the nominal saturation level, due to the extremely short duration at which this condition occurs. Nevertheless for analytical purposes, this current level is still defined as the theoretical saturation threshold within the simulation this is done to facilitate analysis.

As previously noted, a voltage step of 4.9 V is highly unrealistic and would not occur under normal operating conditions. Should such a step ever arise, it would likely

indicate the presence of more critical underlying issues within the system. However, for the purpose of this analysis, the 4.9 V step is applied to evaluate the maximum offset the system can tolerate.

It is clear that the system remains within stable operating conditions, even under this extreme step input, highlighting the robustness of the controllers as the transformer reaches saturation before any signs of instability appears. It can also be noted that tI'_m still reaches a steady state within 10 ms.

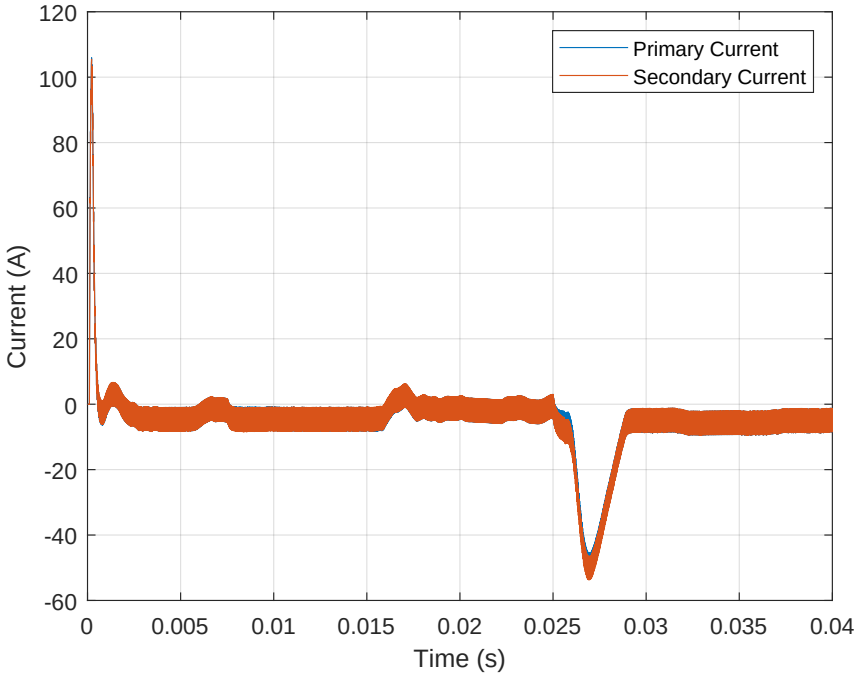

Figure 4.31: Simulated currents for case 3

As observed, I'_p and I'_s rapidly rise to unrealistic levels when the 4.9 V step is applied. The main reason the current is not constrained within reasonable limits is the magnitude of the step input, which causes the dead-time implementation to saturate reaching its maximum output shortly after the step is applied.

Once the dead-time implementation reaches its maximum output, it maintains this while the DC-offset controller continues to integrate the error. Due to the extremely large current values, the DC-offset controller integrates a larger error, allowing it to drive the currents back to zero more quickly than expected. In practice, such a large rise would not occur due to parasitic elements and losses in the transformer, which as previously discussed are not included in the simulation model. However, even with these practical limitations, the current could still reach high levels that may cause significant efficiency losses or damage system components. It is worth noting that even under these unrealistic conditions, the controller successfully drives the currents back to zero within an acceptable time frame. Showcasing the robustness of the control.

This establishes 4.9 V as the maximum offset the system can tolerate under worst-case operating conditions, as identified through the parameter sweep. This total offset could result from a combination of sources within the system. As shown in the sensitivity analysis, dc offset due to temperature could account for a measurement error of 57.61 mA alone. By subtracting this error from the maximum step, we determine the remaining current margin that the system can safely handle before reaching saturation.

4.9 Results from hybrid control

To compare the hybrid control approach, all controllers were implemented in the continuous domain, while sampling frequencies were applied to the corresponding voltage and current measurements. In Figure 4.32, the resulting I'_m is shown. The system response is similar to that of case 1. However, upon closer examination, the hybrid control approach appears to be slightly faster than Case 1 and is also able to restrict the rise in current more effectively, resulting in lower peak values for all three steps: 0.1542 A, −0.1769 A, and 0.6039 A, respectively. Figure 4.33 compares the standard and hybrid cases during the largest current step. It is shown that the peak decreases by 31.764 mA, corresponding to a 4.996 % reduction. This approach highlights the impact of sampling rate on the efficiency of the control and demonstrates the benefits of implementing a hybrid control strategy.

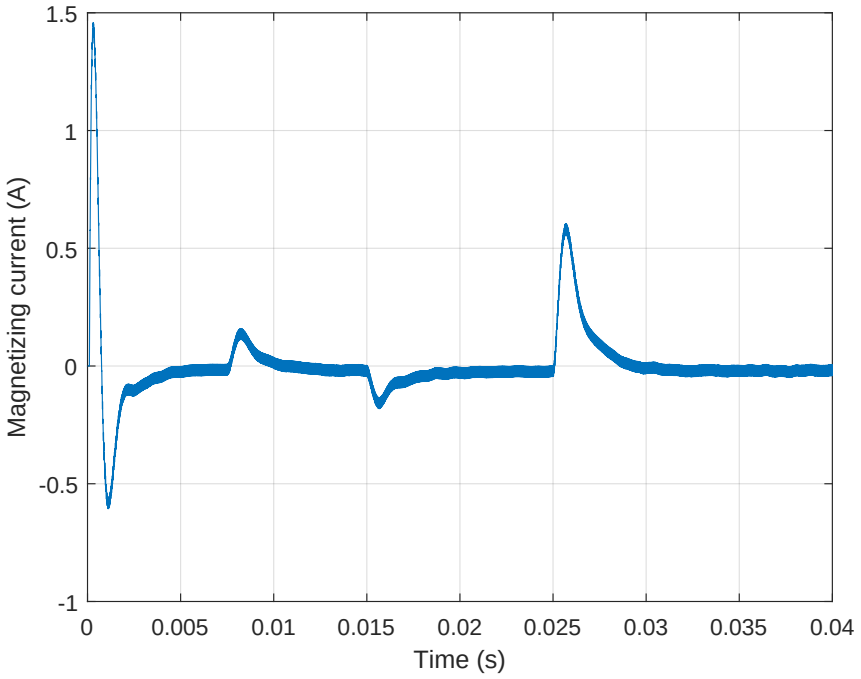

Figure 4.32: Simulated magnetizing current response for the hybrid control

This hybrid approach also seems to have slightly less oscillations than case 1 as seen

in both the early parts as well as the end of the simulation when approaching zero. Even including the decrease in oscillations this approach would most likely still be unrealistic to implement in hardware, as it would require two different measurement setups, significantly increasing the cost. A more cost-effective solution would likely involve investing in higher quality current sensors rather than implementing two separate measurement and control systems. This, combined with the fact that voltage measurement cannot be used on its own, due to its inability to detect steady-state errors caused by the integration required, further supports that this approach is only viable in simulation. Hence, it would likely increase both the complexity and the cost significantly to implement in hardware. These tradeoffs coupled with the lack of providing a more noticeable improvement in performance most likely makes implementation undesirable. To achieve better results, alternative strategies such as using different types of high-pass filters or amplifying the integrated voltage signal may be more effective. Retuning the controllers to match the new system response might also yield better results. However, these alternatives were not explored in depth or prioritized in this study.

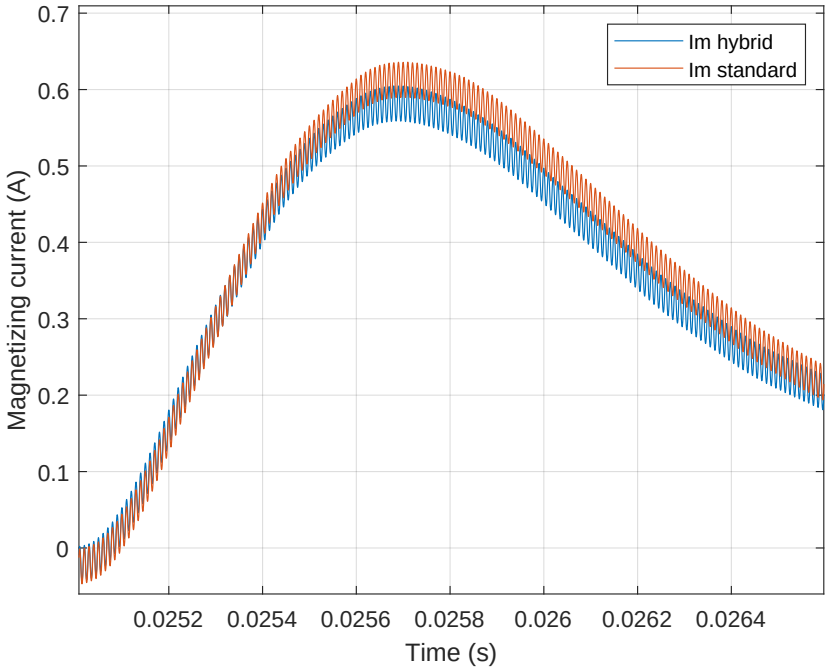

Figure 4.33: Comparison between hybrid and standard control

4.10 Ethical and environmental aspects

It is important to consider environmental and ethical factors when developing power electronic systems, particularly in the context of increasing global demand for energy-efficient and sustainable technologies. As engineers, we not only strive for performance and reliability, but also carry a responsibility to minimize the environmental impact of our designs. This is especially relevant when proposing new control strategies, where the balance between system complexity, performance gain, and environmental footprint must be evaluated.

One of the key advantages of active flux balancing in a PSFB-DAB converter is its effectiveness in reducing magnetizing current and mitigating core flux accumulation. This significantly decreases the risk of transformer core saturation, which in turn reduces thermal and electrical stress on the transformer. A lower operating current contributes to reduced operating temperatures, thereby extending the lifespan not only of the transformer but also of surrounding components exposed to the same thermal environment. Prolonging component lifetimes reduces the amount of replacement components, ultimately contributing to lower electronic waste and improved sustainability.

When implemented effectively, this control strategy enhances overall system efficiency by correcting flux imbalances and minimizing losses associated with core saturation and increased ripple currents. Higher efficiency directly correlates with reduced energy consumption over the converter's lifetime, thereby lowering its environmental footprint. The bidirectional power flow in PSFB-DAB converters also allows for power saving through for example regenerating power when a machine needs to break which could be used to feed energy back into the battery. This also enhances system efficiency by utilizing energy that would otherwise be wasted.

Active flux balancing also eliminates the need for passive balancing, which often relies on large DC-blocking capacitors. As a result, the environmental impact is reduced by decreasing the demand for these components, thereby lowering material depletion and carbon dioxide emissions involved in extraction and production.

5
Conclusion

To conclude this thesis, the implementation of active flux balancing on a PSFB-DAB converter equipped with a planar transformer was investigated. The magnetizing current of the transformer was modeled using a state-space approach and together with two controllers, was used to make slight adjustments to the primary and secondary voltages using the converter's duty cycles to prevent transformer saturation. Several alternative flux balancing methods were also presented and discussed, along with their respective advantages and disadvantages.

It can be concluded from the three variable sweep that the voltage ratio between the primary and secondary side affects the average magnetizing current, I'_m, peaks much more compared to the phase shift. The phase shift does however effect the initial magnitude of the average primary and secondary currents, I'_p and I'_s, significantly. The worst case operating condition was defined to $V_p = 850\,\mathrm{V}$, $V_s = 550\,\mathrm{V}$ and a phase shift of $-90\,^\circ$.

The sensitivity analysis indicates that the saturation limit of the magnetizing current could be reached more easily depending on the temperature difference between the amplification circuits. The analysis revealed that temperature differences between the two current measurement paths represent the dominant source of error in magnetizing current estimation. The influence of component tolerances is small and is further reduced following the initial calibration performed at system startup. The resulting total worst case measurement error was calculated to be $57.61\,\mathrm{mA}$, which in simulation corresponds to a $2.88\,\%$ of the magnetizing current during the maximal step applied.

As demonstrated in the worst-case scenario, the system is capable of handling significant voltage fluctuations of $4.9\,\mathrm{V}$, which would typically be considered very excessive for this application. The results also depend on the measurement resolution of the sensing system. However, robust and stable performance was achieved even with relatively low resolution.

The hardware results confirm that the implemented control works effectively in both theory and practice. Although the simulation model has a $1.6257\,\mathrm{s}$ shorter rise time, corresponding to a $48.99\,\%$ faster response, the hardware still demonstrates a robust and reliable step response coupled with a simulation model that is representative of the hardware.

The hybrid control implementation resulted in the best step response mitigation for I'_m. Although the hybrid measurement system provided an improvement, the difference was not significant enough to justify its inclusion in hardware. Adding the hybrid measurement would most likely not be cost-effective, as the increase in performance likely does not outweigh the added cost and complexity of the required additional sensing system.

5.1 Future work

There are several areas that would be interesting to explore as future work based on the results of this thesis. One area that might be worth exploring is the hybrid control system. While it did not show a significant enough improvement in this application to justify its inclusion, future work could involve a more in depth analysis of the PI controllers with the hybrid approach in mind. By tuning the controllers together as a single system, including the hybrid control system, it may be possible to improve the overall performance. It does however remain limited by the requirement of two different sensing systems. Control using the integral of the voltages is however still an interesting proposal.

To further improve the implemented simulation model, it would be valuable to investigate the inclusion of parasitic elements and resistances in the state-space model, along with the implementation of losses, to achieve a more realistic simulated control response that better reflects behavior in hardware.

One potential improvement would be to refine the tuning of the DC-offset controller. Currently, the dead-time effect limits the current magnitude, reducing the signal available for integration and leading to a slower response. A tuning method that accounts for the dead-time effect was not implemented due to time constraints, but it would nevertheless be an interesting subject for further development.

Another area for further investigation is the dead-time implementation within the Simulink model. The current model is very basic and simplified. Modeling a more accurate representation of the dead-times effect in the actual hardware could lead to more precise simulation results. Additionally, it would also be very interesting to continue exploring the possibility of using dead-time to prevent saturation. This could involve designing a control circuit that dynamically adjusts dead-time. The impact of this adjustment on system performance, power distribution, and overall efficiency would need to be carefully assessed. It would be important to evaluate if the potential benefits of adjusting dead-time outweigh the losses it might cause, especially in terms of efficiency and power distribution. It does however present a very interesting subject and has already proven its ability to limit the magnetizing flux. If such a dead-time control approach proves effective, it would also be interesting to assess whether all existing controllers would still be necessary, or if some could be removed.

Bibliography

[1] B. Mangu, S. Akshatha, D. Suryanarayana, and B. G. Fernandes, "Grid-connected pv-wind-battery-based multi-input transformer-coupled bidirectional dc-dc converter for household applications," *IEEE Journal of Emerging and Selected Topics in Power Electronics*, vol. 4, no. 3, pp. 1086–1095, 2016. DOI: 10.1109/JESTPE.2016.2544789.

[2] R. K. Kanaparthi, J. P. Singh, and M. S. Ballal, "A review on multi-port bidirectional isolated and non-isolated dc-dc converters for renewable applications," in *2022 IEEE International Conference on Power Electronics, Drives and Energy Systems (PEDES)*, 2022, pp. 1–6. DOI: 10.1109/PEDES56012.2022.10080049.

[3] F. Krismer, "Modeling and optimization of bidirectional dual active bridge dc-dc converter topologies," en, Diss, Swiss Federal Institute of Technology ETH Zurich, No. 19177, 2010., Doctoral Thesis, ETH Zurich, Zurich, 2010. DOI: 10.3929/ethz-a-006395373.

[4] D. Costinett, D. Maksimovic, and R. Zane, "Design and control for high efficiency in high step-down dual active bridge converters operating at high switching frequency," *IEEE Transactions on Power Electronics*, vol. 28, no. 8, pp. 3931–3940, 2013. DOI: 10.1109/TPEL.2012.2228237.

[5] B. Zhao, Q. Song, W. Liu, and Y. Zhao, "Transient dc bias and current impact effects of high-frequency-isolated bidirectional dc–dc converter in practice," *IEEE Transactions on Power Electronics*, vol. 31, no. 4, pp. 3203–3216, 2016. DOI: 10.1109/TPEL.2015.2445831.

[6] J. Wen, H. Wen, and Q. Bu, "An optimal control for dual-active-bridge dc-dc converter in eliminating transient dc bias current," in *2019 IEEE 10th International Symposium on Power Electronics for Distributed Generation Systems (PEDG)*, 2019, pp. 849–852. DOI: 10.1109/PEDG.2019.8807617.

[7] Z. Ouyang and M. A. E. Andersen, "Overview of planar magnetic technology—fundamental properties," *IEEE Transactions on Power Electronics*, vol. 29, no. 9, pp. 4888–4900, 2014. DOI: 10.1109/TPEL.2013.2283263.

[8] R. C. Fernow, *Principles of Magnetostatics*. Cambridge University Press, 2016.

[9] T. Nakajima, K.-I. Suzuki, M. Yajima, N. Kawakami, K.-I. Tanomura, and S. Irokawa, "A new control method preventing transformer dc magnetization for voltage source self-commutated converters," *IEEE Transactions on Power Delivery*, vol. 11, no. 3, pp. 1522–1528, 1996. DOI: 10.1109/61.517512.

[10] S. Han, I. Munuswamy, and D. Divan, "Preventing transformer saturation in bi-directional dual active bridge buck-boost dc/dc converters," in *2010 IEEE*

Energy Conversion Congress and Exposition, 2010, pp. 1450–1457. DOI: 10.1109/ECCE.2010.5618254.

[11] G. Ortiz, L. Fässler, J. W. Kolar, and O. Apeldoorn, "Flux balancing of isolation transformers and application of "the magnetic ear" for closed-loop volt–second compensation," *IEEE Transactions on Power Electronics*, vol. 29, no. 8, pp. 4078–4090, 2014. DOI: 10.1109/TPEL.2013.2294551.

[12] J. Muhlethaler, J. Biela, J. W. Kolar, and A. Ecklebe, "Core losses under the dc bias condition based on steinmetz parameters," *IEEE Transactions on Power Electronics*, vol. 27, no. 2, pp. 953–963, 2012. DOI: 10.1109/TPEL.2011.2160971.

[13] R. T. Naayagi, A. J. Forsyth, and R. Shuttleworth, "High-power bidirectional dc–dc converter for aerospace applications," *IEEE Transactions on Power Electronics*, vol. 27, no. 11, pp. 4366–4379, 2012. DOI: 10.1109/TPEL.2012.2184771.

[14] J. Deng and H. Wang, "A hybrid-bridge and hybrid modulation-based dual-active-bridge converter adapted to wide voltage range," *IEEE Journal of Emerging and Selected Topics in Power Electronics*, vol. 9, no. 1, pp. 910–920, 2021. DOI: 10.1109/JESTPE.2019.2949604.

[15] Y. Panov, M. M. Jovanović, L. Gang, and M. Yueyong, "Transformer-flux-balancing control in isolated bidirectional dc-dc converters," in *2014 IEEE Applied Power Electronics Conference and Exposition - APEC 2014*, 2014, pp. 49–56. DOI: 10.1109/APEC.2014.6803288.

[16] P. Yao, X. Jiang, P. Xue, S. Ji, and F. Wang, "Flux balancing control of ungapped nanocrystalline core-based transformer in dual active bridge converters," *IEEE Transactions on Power Electronics*, vol. 35, no. 11, pp. 11 463–11 474, 2020. DOI: 10.1109/TPEL.2020.2984789.

[17] S. Klopper and J. Ferreira, "A sensor for balancing flux in converters with a high frequency transformer link," in *Conference Record of the 1993 IEEE Industry Applications Conference Twenty-Eighth IAS Annual Meeting*, 1993, 1315–1320 vol.2. DOI: 10.1109/IAS.1993.299111.

[18] R. Patel, "Detecting impending core saturation in switched-mode power converters," in *Proc. 7th Nat. Solid-State Power Convers. Conf.*, vol. B3, Mar. 1980, pp. 1–11.

[19] D. Wilson, "A new pulsewidth modulation method inherently maintains output transformer flux balance," in *Proc. 8th Nat. Solid-State Power Convers. Conf.*, vol. D1, Apr. 1981, pp. 1–14.

[20] S. Ziegler, R. C. Woodward, H. H.-C. Iu, and L. J. Borle, "Current sensing techniques: A review," *IEEE Sensors Journal*, vol. 9, no. 4, pp. 354–376, 2009. DOI: 10.1109/JSEN.2009.2013914.

[21] The MathWorks, Inc., *Simulink*, The MathWorks, Inc., 2024. [Online]. Available: https://www.mathworks.com/products/simulink.html.

[22] The MathWorks, Inc., *Simulink® getting started guide*, The MathWorks, Inc., 2024. [Online]. Available: https://se.mathworks.com/help/releases/R2024b/pdf_doc/simulink/simulink_gs.pdf.

[23] Analog Devices, Inc., *Ltspice*, Analog Devices, Inc., 2025. [Online]. Available: https://www.analog.com/en/resources/design-tools-and-calculators/ltspice-simulator.html.

[24] *Spice simulation*, Cadence Design Systems Inc., 2025. [Online]. Available: https://www.cadence.com/en_US/home/explore/spice-simulation.html.

[25] *Get up and running with ltspice*, Analog Devices, Inc., 2025. [Online]. Available: https://www.analog.com/media/en/analog-dialogue/volume-53/number-4/get-up-and-running-with-ltspice.pdf.

[26] *Bode analyzer suite*, OMICRON Lab, 2024. [Online]. Available: https://www.omicron-lab.com/products/vector-network-analysis/bode-analyzer-suite/page#.

[27] OMICRON Lab, *Vector network analyzer - bode 100*. [Online]. Available: https://www.omicron-lab.com/products/vector-network-analysis/bode-100#.

[28] OMICRON Lab, *Bode 100 - application note, transformer modelling*. [Online]. Available: https://www.omicron-lab.com/fileadmin/assets/Bode_100/ApplicationNotes/Transformer_modelling/App_Note_Transformer_modelling_V_2_0.pdf.

[29] *Bode 100$_u$sermanual*, OMICRON Lab, 2023. [Online]. Available: https://www.datatec.eu/media/71/89/72/1718751482/OMICRON%20Lab-Bode100-HB-1_DE_(1).pdf?ts=1718751482.

[30] G. s. Fishman, *Monte Carlo: Concepts, Algorithms and Applications*. Springer-Verlag New York, 1996.

[31] T. Glad and L. Ljung, *Control Theory: Multivariable and Nonlinear Methods*. Taylor Francis, 2000.

[32] B. Lennartsson, *Reglerteknikens grunder*, 4th ed. Lund: Studentlitteratur, 2000.

DEPARTMENT OF ELECTRICAL ENGINEERING
CHALMERS UNIVERSITY OF TECHNOLOGY
Gothenburg, Sweden
www.chalmers.se

CHALMERS
UNIVERSITY OF TECHNOLOGY